



1 **Bio-optical characterization of subsurface chlorophyll maxima in**
2 **the Mediterranean Sea from a Biogeochemical-Argo float**
3 **database**

4 Marie Barbieux¹, Julia Uitz¹, Bernard Gentili¹, Orens Pasqueron de Fommervault², Alexandre Mignot³, Antoine Poteau¹,
5 Catherine Schmechtig⁴, Vincent Taillandier¹, Edouard Leymarie¹, Christophe Penkerc'h¹, Fabrizio D'Ortenzio¹, Hervé
6 Claustre¹ & Annick Bricaud¹

7 ¹CNRS and Sorbonne Université, Laboratoire d'Océanographie de Villefranche, LOV, F-06230 Villefranche-sur-mer, France

8 ²Alseamar-alcen company, 9 Europarc Sainte Victoire, 13590 Meyreuil, France

9 ³Mercator Océan, 31520 Ramonville Saint Agne

10 ⁴OSU Ecce Terra, UMS 3455, CNRS and Sorbonne Université, Paris 6, 4 place Jussieu 75252 Paris cedex 05, France

11

12 *Correspondence to:* Marie Barbieux (marie.barbieux@obs-vlfr.fr)

13 **ABSTRACT**

14 As commonly observed in oligotrophic stratified waters, a Subsurface (or Deep)
15 Chlorophyll Maximum (SCM) frequently characterizes the vertical distribution of
16 phytoplankton chlorophyll in the Mediterranean Sea. Occurring far from the surface layer
17 “seen” by ocean color satellites, SCMs are difficult to observe with adequate spatio-temporal
18 resolution and their biogeochemical impact remains unknown. BioGeochemical-Argo (BGC-
19 Argo) profiling floats represent appropriate tools for studying the dynamics of SCMs. Based
20 on data collected from 36 BGC-Argo floats deployed in the Mediterranean Sea, our study
21 aims to address two main questions: (1) What are the different types of SCMs in
22 Mediterranean Sea? (2) Which environmental factors control their occurrence and dynamics?
23 First, we analyzed the seasonal and regional variations of the chlorophyll concentration
24 (*Chla*), particulate backscattering coefficient (b_{bp}), a proxy of the Particulate Organic Carbon
25 (POC), and environmental parameters (PAR and nitrates) within the SCM layer over the
26 Mediterranean basin. The vertical profiles of *Chla* and b_{bp} were then statistically classified,
27 and the seasonal occurrence of each of the different types of SCMs quantified. Finally, a case
28 study was performed on two contrasted regions and the environmental conditions at depth
29 were further investigated to understand which parameter controls the SCMs. In the Eastern
30 Basin, SCMs result, at a first order, from photoacclimation process. Conversely, SCMs in the
31 Western Basin reflect a biomass increase at depth benefiting from both light and nitrate
32 resources. Our results also suggest that a variety of intermediate types of SCMs are
33 encountered between these two end-member situations.



34 1 INTRODUCTION

35 The vertical distribution of phytoplankton in the open ocean is often characterized by
36 the occurrence of high chlorophyll *a* concentration (Chl*a*) beneath the mixed layer (Cullen
37 and Eppley, 1981; Fasham et al., 1985; Raimbault et al., 1993; Letelier et al., 2004; Tripathy
38 et al., 2015). This phenomenon is commonly referred to as Deep Chlorophyll Maximum
39 (DCM) or Subsurface Chlorophyll Maximum (SCM). Although it always happens below the
40 surface layer (approximately below the first 20 meters), it does not necessarily settle very
41 deep in the water column, thus making the notation DCM sometimes inappropriate. Hence, in
42 the following, we will use the notation SCM. Commonly observed at depth in oligotrophic
43 stratified regions (Anderson, 1969; Cullen, 1982; Furuya, 1990; Mignot et al., 2014), SCMs
44 are also known to occur below the mixed layer in temperate- and high-latitude environments
45 (Parslow et al., 2001; Uitz et al., 2009; Ardyna et al., 2013; Arrigo et al., 2011). The
46 formation of a subsurface maximum of Chl*a* in these different ecosystems results from
47 various underlying mechanisms leading to different types of SCMs. In stratified waters,
48 SCMs often result from photoacclimation of the phytoplankton organisms, which induces an
49 increase in the intracellular Chl*a* in response to low light conditions (Dubinsky and Stambler,
50 2009; Fennel and Boss, 2003; Kiefer et al., 1976; Winn et al., 1995). However SCMs
51 resulting from an actual increase in phytoplankton carbon biomass have also been reported in
52 such ecosystems (Beckmann and Hense, 2007; Crombet et al, 2011; Mignot et al., 2014). In
53 high-latitude regions with well-mixed surface waters, SCMs have been shown to result from
54 the accumulation of particles sinking from the mixed layer (Quéguiner et al., 1997; Parslow et
55 al, 2001), photophysiological acclimation of algal cells (Mikaelyan and Belyaeva, 1995) or
56 phytoplankton growth at the depth of the nutricline (Holm-Hansen and Hewes, 2004; Tripathy
57 et al, 2015). Hence, regional or local studies have highlighted underlying processes indicating
58 that, under certain conditions, SCMs could contribute to carbon production and export, and



59 thus potentially have an important biogeochemical role. However, we have limited knowledge
60 of their biogeochemical significance at large spatial and temporal scales. Their contribution to
61 the depth-integrated primary production has been assessed for a limited number of regions
62 and remains largely unknown, although it has been reported to be underestimated from 40 to
63 75% in the Arctic Ocean (Ardyna et al, 2013; Hill et al, 2013). The biogeochemical
64 contribution of the SCMs to the global ocean is also particularly hard to assess at large spatio-
65 temporal scales, especially because SCMs settle at a depth usually far from the surface layer
66 “seen” by ocean color satellites. Remotely sensed estimates are restricted to the upper layer
67 of the water column that represent only one fifth of the euphotic layer where phytoplankton
68 photosynthesis takes place (Gordon and McCluney, 1975). The exact biogeochemical role of
69 SCMs, thus, needs to be further explored.

70 The Mediterranean Sea is considered as an oligotrophic province where the vertical
71 distribution of phytoplankton is, seasonally or permanently, characterized by the occurrence
72 of a SCM (Christaki, 2001; Estrada et al., 1993; Kimor et al., 1987; Lavigne et al., 2015;
73 Siokou-Frangou et al., 2010; Videau et al., 1994). It is also a low-nutrient concentration basin,
74 one of the largest nutrient-depleted areas of the global ocean and it is characterized by a west-
75 to-east gradient in both nutrients and chlorophyll *a* concentration (Dugdale and Wilkerson,
76 1988; Bethoux et al., 1992; Antoine et al., 1995; Bosc et al., 2004; D’Ortenzio and Ribera
77 d’Alcalà, 2009). While the Eastern Basin is defined as oligotrophic (Krom et al., 1991;
78 Ignatiades et al., 2002; Lavigne et al., 2015), the Western Basin is more productive and
79 behaves as a temperate system (Morel and André, 1991; Marty et al., 2002; Mayot et al.,
80 2017b). Hence, this “miniature ocean” presents SCMs that may be encountered in both
81 temperate environments and stratified waters of the global ocean. This, coupled with an
82 intensive effort of biogeochemical observations in this region, makes the Mediterranean Sea
83 an ideal region for studying SCMs.



84 The biogeochemical and bio-optical community recently developed autonomous
85 profiling floats that collect *in situ* vertical profiles of biogeochemical properties such as the
86 chlorophyll *a* fluorescence (*i.e.* a proxy of the chlorophyll *a* concentration (Chl*a*)) and the
87 particulate backscattering coefficient (b_{bp}) (*i.e.* a proxy of the Particulate Organic Carbon
88 (POC)). Physical-chemical properties such as nitrate concentration ($[NO_3^-]$) or the
89 Photosynthetically Available Radiation (PAR), essential to understand the functioning of
90 SCMs, are also measured simultaneously (Johnson et al., 2009; Claustre et al., 2010; Johnson
91 and Claustre, 2016). Thirty-six BioGeochemical-Argo (BGC-Argo) have been deployed in the
92 Mediterranean Sea from 2012 to 2017, providing a database of 4050 *in situ* multi-variable
93 profiles. This extensive database gives us the unique opportunity to enhance our
94 comprehension of the vertical distribution and seasonal variability of the phytoplankton
95 biomass in the subsurface layer of the Mediterranean Sea and expand our understanding of the
96 mechanisms involved in the occurrence of SCMs. Our study seeks to address two main
97 questions: (1) What are the different types of SCMs in Mediterranean Sea?; and (2) Which
98 environmental factors control the occurrence and dynamics of the different types of SCMs in
99 this region? To address these questions, three complementary approaches were used. First,
100 based on a climatological approach, we analyzed the spatial and seasonal variability of
101 biogeochemical properties (*i.e.* Chl*a* and b_{bp}) and environmental conditions at the SCM level.
102 This should lead to the identification of the main mechanisms controlling SCMs in different
103 regions of the Med Sea. Second, using a statistical method, we classified the vertical profiles
104 of Chl*a* and b_{bp} seasonally encountered in the various regions of the Med. This approach
105 allowed us to quantify the frequency of occurrence of distinct types of SCMs in these
106 different regions. Finally, using two specific BGC-Argo floats deployed in the Gulf of Lions
107 and the Levantine Sea, we conducted a case study of two contrasted regimes and investigate
108 the environmental conditions that control the occurrence of SCMs in each regime.



109 2 DATA AND METHODS

110 2.1 The BGC-Argo profiling float database

111 Thirty-six BGC-Argo profiling floats were deployed in the Mediterranean Sea in 5
112 geographic areas, *i.e.* the Northwestern (NW) and Southwestern (SW) regions, the Tyrrhenian
113 (TYR), Ionian (ION) and Levantine (LEV) Seas. Our study was based on the analysis of a
114 database comprising 4050 multivariable vertical profiles, corresponding to upward casts
115 collected between November 26, 2012 and September 27, 2017 (Table 1 and Figure 1). The
116 “PROVOR CTS-4” (NKE Marine Electronics, Inc.) is a profiling autonomous platform that
117 has been specifically designed in the frame of the remOcean and NAOS projects. The
118 physical variables (depth, temperature and salinity) were acquired by a SBE 41 CTD (Sea-
119 Bird Scientific Inc.). Two optical packages, the so-called remA and remB, were developed to
120 be specifically implemented on profiling floats. The remA is composed of an OCR-504
121 (SATLANTIC, Inc.), a multispectral radiometer that measures the Photosynthetically Available
122 Radiation (PAR) and the downwelling irradiance at 380, 410 and 490 nm. The remA also
123 includes an ECO3 sensor (Combined Three Channel Sensors; WET Labs, Inc.) measuring the
124 fluorescence of the chlorophyll *a* and the Colored Dissolved Organic Matter (CDOM) at
125 excitation/emission wavelengths of 470/695 nm and 370/460 nm, respectively, and the
126 angular scattering coefficient of particles ($\beta(\theta, \lambda)$) at 700 nm and at an angle of 124°. Finally,
127 15 floats were also equipped with a nitrate (NO_3^-) (Deep SUNA, Sea-Bird Scientific, Inc.)
128 or/and an oxygen (O_2) sensor (optode 4330, Aanderaa, Inc.). Depending on the scientific
129 objectives of the different projects, the measurements were collected during upward casts
130 programmed every 1, 2, 3, 5, or 10 days. All casts started from a parking depth at 1000 m at a
131 time that was sufficient for surfacing around local noon. The vertical resolution of data
132 acquisition was 10 m between 1000 m and 250 m, 1 m between 250 m and 10 m, and 0.2 m



133 between 10 m and the surface. Each time the floats surfaced, the raw data were transmitted to
134 land through Iridium two-way communication.

135 **2.2 Retrieval of key biogeochemical variables from optical measurements**

136 For each bio-optical parameter, raw counts were converted into the desired quantities
137 according to technical specifications and calibration coefficients provided by the
138 manufacturer. These quantities were transformed into chlorophyll *a* concentration (*Chl_a*) and
139 particulate backscattering coefficient (*b_{bp}*) following the BGC-Argo procedure (Schmechtig et
140 al., 2015, 2016b). In addition, we applied a global factor of 2 to correct chlorophyll *a*
141 fluorescence measurements from WET Labs ECO fluorometers, following the
142 recommendation of Roesler et al. (2017). This correction factor applied to BGC-Argo data
143 was found to have little impact on the interpretation of the results on a global scale (Barbieux
144 et al., 2018; Organelli et al., 2017) and did not modify the interpretation of the present results,
145 especially because the regional correction factors proposed by Roesler et al. (2017) for the
146 Mediterranean Sea are very close to the global factor of 2 (1.62 and 1.72 for the Western and
147 Eastern Basin, respectively). Finally a quality-controlled procedure was performed following
148 the BGC-Argo recommendations (Schmechtig et al., 2016a). All data were also visually
149 checked in order to detect any drift over time or sensor deficiency. These data were made
150 freely available by the International Argo Program ([http:// www.argo.ucsd.edu](http://www.argo.ucsd.edu),
151 <http://argo.jcommops.org>) and the CORIOLIS project (<http://www.coriolis.eu.org>).

152 After binning the data at a 1-m resolution, the mixed layer depth (MLD) was derived
153 from the CTD data using a 0.03 kg m^{-3} density criterion (de Boyer Montégut, 2004). The
154 depth of the SCM and of the Subsurface *b_{bp}* Maximum (*Sb_{bp}M*) was identified as the depth
155 where the absolute value of *Chl_a* or *b_{bp}* reaches a maximum below the MLD. Large spikes
156 associated with particle aggregates or zooplankton (Gardner et al., 2000; Briggs et al., 2011)



157 were observed in the b_{bp} profiles and made it sometimes difficult to identify the depth of the
158 $S_{b_{bp}M}$. Hence, for the purpose of the $S_{b_{bp}M}$ retrieval exclusively, the b_{bp} values were
159 smoothed with a mean filter (5-point window). To study the SCM dynamics and obtain the
160 width of the SCM that may fluctuate in space and time, a Gaussian profile was adjusted to
161 each *Chla* vertical profile of the database that presented a SCM. This approach first proposed
162 by Lewis et al. (1983) has been widely used in oceanographic studies (e.g. Morel and
163 Berthon, 1989; Uitz et al., 2006; Barbieux et al., 2017). The width of the gaussian adjusted to
164 the vertical profile of *Chla* represented the width of the SCM. The SCM layer was defined as
165 the layer extending across the entire width of the SCM. The upper (or lower) limit was
166 retrieved by removing (or adding) half of the width of the SCM to the absolute depth of the
167 SCM.

168 **2.3 Estimation of nitrate concentration**

169 The SUNA sensor measures the light absorption in the wavelength range from 217 to
170 240 nm. In this spectral band, the light absorption is dominated by nitrates and bromides, and,
171 to a much lesser extent, by organic matter (Johnson and Coletti, 2002). Various algorithms
172 were developed to obtain the nitrate concentration ($[NO_3^-]$) from the measured light
173 absorption spectrum (e.g. Arai et al., 2008; Zielinski et al., 2011). The TCSS algorithm was
174 specifically developed to take into account the temperature dependency of the bromide
175 spectrum, which significantly improved the accuracy of the retrieved $[NO_3^-]$ (Sakamoto et al.,
176 2009). This algorithm was recently modified to also take into account a pressure dependency
177 (Pasqueron de Fommervault et al., 2015a; Sakamoto et al., 2017). Previous studies also
178 evidenced the inaccuracy of standard calibration procedures (D'Ortenzio et al., 2014;
179 Pasqueron de Fommervault et al., 2015a) and showed that SUNA sensors often undergo offset
180 issue and drift over time (Johnson and Coletti, 2002). Johnson et al. (2017) proposed a
181 method to correct these issues for the Southern Ocean. Using the GLODAP-V2 database



182 (<http://cdiac.ornl.gov/oceans/GLODAPv2>) of *in situ* measurements, the authors determined an
183 empirical relationship allowing the estimation of the $[\text{NO}_3^-]$ at depth ($[\text{NO}_3^-]_{\text{deep_pred}}$ for
184 nitrate concentration deep reference value) using a multiple linear regression (MLR) with
185 physical and geolocation parameters as predictors (salinity, temperature, oxygen, latitude and
186 longitude). BGC-Argo profiles of nitrate concentration were then corrected by adjusting the
187 SUNA measurements to the retrieved deep reference value. Following a similar approach, we
188 established a regional empirical relationship for the Mediterranean Sea (Eq.1) allowing to
189 retrieve the $[\text{NO}_3^-]_{\text{deep_pred}}$ values using parameters that were systematically measured by
190 the BGC-Argo floats (*i.e.* latitude, longitude, temperature and salinity). For the Mediterranean
191 Sea, oxygen was not used as an input parameter of the MLR as this parameter was not
192 systematically available for the BGC-Argo floats of our database. Moreover, its absence in
193 the MLR as an input parameter did not affect the retrieval of the nitrate concentrations.
194 Comparing the nitrate concentrations predicted by the MLR to the nitrate concentrations from
195 GLODAP-V2 data, the determination coefficients of the relationship presented very similar
196 values for the model with and without oxygen (see Figure S1 in Supplement 1).

197 Hence, the following equation was finally used:

$$198 \quad [\text{NO}_3^-]_{\text{deep_pred}} = 454.28 - 0.002 \times \text{Latitude} - 0.0473 \times \text{Longitude} + 1.7262 \times \text{Temperature} - \\ 199 \quad 12.165 \times \text{Salinity} \quad (1)$$

200 A strong correlation was noticed between the nitrate concentrations predicted from the MLR
201 model and the measurements provided in the GLODAP-V2 database. This correlation was
202 associated with a strong determination coefficient ($R^2 = 0.89$) and a small root mean square
203 error (RMSE = $0.52 \mu\text{mol L}^{-1}$). Then, comparing the predicted climatology-based with the



204 observed BGC-Argo nitrate concentrations at depth and computing the adjusted nitrate
205 concentration for each depth, we obtained the following equation:

$$206 \quad [\text{NO}_3^-]_{\text{adjusted}}(t,z) = [\text{NO}_3^-]_{\text{raw}}(t,z) - ([\text{NO}_3^-]_{\text{deep_obs}}(t) - [\text{NO}_3^-]_{\text{deep_pred}}(t)) \quad (2)$$

207 with $[\text{NO}_3^-]_{\text{raw}}(t,z)$ corresponding to the raw nitrate value from the SUNA sensor.

208 The BGC-Argo $[\text{NO}_3^-]$ profiles of the Mediterranean database were compared with *in*
209 *situ* measurements collected simultaneously to float deployment (see Taillandier et al., 2017
210 for more details), using the classic colorimetric method (Morris and Riley, 1963). We
211 demonstrated that the retrieval of the BGC-Argo $[\text{NO}_3^-]$ with the proposed calibration
212 procedure was satisfying. The comparison between the nitrate concentrations retrieved from
213 the BGC-Argo floats to the reference *in situ* measurements (Figure 2) showed a robust
214 relationship ($R^2 = 0.86$ and slope = 0.97, $N = 162$).

215 The nitracline that separates upper nitrate-depleted waters from lower repleted waters
216 corresponds, in this paper, to the depth where $[\text{NO}_3^-]$ is 1 μM smaller than the median $[\text{NO}_3^-]$
217 value in the first 10 meters of the water column (Lavigne et al., 2013). The diffusive vertical
218 supply of nitrates to the euphotic zone is not only influenced by the depth of the nitracline
219 from the sunlit surface layer but also by the slope of the nitracline. The slope of the nitracline
220 was calculated as the vertical $[\text{NO}_3^-]$ gradient between the isocline 1 μM and the isocline 3
221 μM as already done for the Mediterranean Sea by Pasqueron de Fommervault et al. (2015a).

222 **2.4 Estimation of daily PAR**

223 The BGC-Argo vertical profiles of PAR were quality-checked following Organelli et al.
224 (2016). Only solar noon profiles were considered for our analysis because zenith
225 measurements ensure the best retrieval (Organelli et al., 2017) of the isolume, *i.e.* depth



226 corresponding to a chosen value of light. BGC-Argo floats provide instantaneous PAR
227 (iPAR) measurements just beneath the sea surface at local noon (iPAR(0⁻, noon)).

228 From iPAR measurement, a vertical profile of daily-averaged PAR was estimated
229 following the method of Mignot et al. (2018). This method relies on a theoretical clear-sky
230 estimate of iPAR just beneath the sea surface using the solar irradiance model SOLPOS
231 developed by the National Renewable Energy Laboratory (NREL, 2000). Hence, we followed
232 three main steps:

233 (1) The instantaneous photosynthetically available radiation just beneath the sea surface at
234 time t , iPAR(0⁻, t) in $\mu\text{mol photons m}^{-2} \text{s}^{-1}$, was determined from Eq. (3):

$$235 \quad \text{iPAR}(0^-, t) = \text{iPAR}_{\text{clear}}(0^-, t) \frac{\text{iPAR}(0^-, \text{noon})}{\text{iPAR}_{\text{clear}}(0^-, \text{noon})} \quad (3)$$

236 with $\text{iPAR}_{\text{clear}}(0^-, t)$ the theoretical estimate of iPAR just beneath the sea surface at time t ,
237 $\text{iPAR}(0^-, \text{noon})$ the float measurement of iPAR just beneath the sea surface at local noon,
238 and $\text{iPAR}_{\text{clear}}(0^-, \text{noon})$ the theoretical estimate of iPAR just beneath the sea surface at local
239 noon for the same time and location as the float measurement. The ratio of $\text{iPAR}(0^-, \text{noon})$ to
240 $\text{iPAR}_{\text{clear}}(0^-, \text{noon})$ represented an index of the cloud coverage at noon, which was applied
241 to the clear-sky iPAR estimates at any time t . This approach thus assumes that the cloud
242 coverage at noon is representative of the daily cloud coverage. Although the cloud coverage is
243 unlikely to be constant throughout the entire day, this approach enabled to account for the
244 daily course of light through modeled estimates, rather than considering only the noon-time
245 instantaneous float measurements.

246 (2) The daily-averaged PAR just beneath sea surface, $\text{PAR}(0^-)$ in $\text{mol photons m}^{-2} \text{d}^{-1}$, was
247 obtained by averaging Eq. (3) over daylength. In parallel, the diffuse attenuation coefficient
248 for PAR, $K_d(\text{PAR})$ in unit of m^{-1} , was derived from the float iPAR measurements by fitting a
249 linear least square regression forced through the origin between the data of



250 $\ln \left(\frac{iPAR_{float}(z, noon)}{iPAR_{float}(0^-, noon)} \right)$ and z taken in the upper 40 m of the water column (Mignot et al.,
251 2018).

252 (3) Finally, the daily-averaged PAR for each depth z of the water column, $PAR(z)$ in units of
253 $\text{mol photons m}^{-2} \text{d}^{-1}$, was calculated from $K_d(PAR)$ and $PAR(0^-)$ as follows:

$$254 \quad PAR(z) = PAR(0^-) \exp(-K_d(PAR)z) \quad (4)$$

255 Additionally, the isolume $0.3 \text{ mol quanta.m}^{-2} \text{d}^{-1}$, which corresponds to the dataset
256 median daily PAR value at the SCM depth, was used as an indicator of the light available for
257 photosynthesis at the SCM level. We also computed the euphotic layer depth (Z_{eu}) as the
258 depth where the PAR is reduced to 1% of its surface value (Gordon and McCluney, 1975) and
259 the penetration depth (Z_{pd}) calculated as $Z_{eu} / 4.6$. The surface layer corresponds to the layer
260 extending from 0 to Z_{pd} .

261 **2.5 Statistical method of classification of the vertical profiles providing the** 262 **identification of the SCM**

263 A statistical method based on the Singular Value Decomposition (SVD) algorithm
264 (Golub and Van Loan, 1996) was used to identify the different types of SCMs in the
265 Mediterranean Sea. The approach allowed to tackle the large amount of data provided by the
266 BGC-Argo floats and to simultaneously classify the $Chla$ and b_{bp} vertical profiles of the
267 database. Based on the shape of the $Chla$ or b_{bp} vertical profile, the method did not require an
268 *a priori* knowledge on the considered profile such as in previous studies (*e.g.* Uitz et al. 2006;
269 Mignot et al., 2011; Lavigne et al., 2015). The present method involved three major steps
270 summarized as follows (see Supplementary Material 2 for more details):

271 (1) Each vertical profile of $Chla$ and b_{bp} were normalized in depth and magnitude. The depths
272 were normalized by the euphotic depth (Z_{eu}) and the $Chla$ and b_{bp} values were normalized to



273 the maximum value of each profile (i.e. $Chl_{a_{max}}$ and $b_{bp_{max}}$, respectively). Ultimately, the
274 Chl_a and b_{bp} values of a profile were joined by one end, to obtain a dimensionless, twice as
275 long, “metaprofile” that was subsequently classified on the basis of its shape.

276 (2) A Principal Component Analysis (PCA) was performed using the Singular Value
277 Decomposition algorithm (Pearson, 1901). The singular values were ordered in decreasing
278 order and only the first N values were kept. N was chosen so that the corresponding singular
279 vectors capture 95% of variance of the dataset and the resulting vertical profiles of Chl_a and
280 b_{bp} were ecologically meaningful (see Supplement 2 provided as electronic supplementary
281 material).

282 (3) Each singular vector defined a profile shape. A dimensionless metaprofile can be
283 represented as a linear combination of those shapes, each multiplied by a coefficient. To
284 classify each metaprofile in a category of shape, we used a numerical optimization algorithm
285 on the whole set of coefficients to maximize the value of one coefficient while minimizing the
286 $N-1$ others, for each metaprofile. The coefficient that was maximal for each metaprofile
287 defined its class of shape. More details on the method are provided as electronic
288 supplementary material.

289 For each of the five regions of the Mediterranean considered, we finally obtained the
290 dominant shapes of vertical Chl_a and b_{bp} profiles, which are representative of the different
291 situations encountered along an annual cycle. This approach allowed to establish a typology
292 of SCMs in the BGC-Argo database and to report their frequency of occurrence in each
293 region.



294 3 RESULTS & DISCUSSION

295 3.1 Regional and seasonal variability of the SCM

296 Using a climatological approach, we first examined the characteristics of the SCMs
297 such as their depth, thickness and amplitude in order to better apprehend their vertical
298 dynamics in the water column along the Mediterranean west-to-east gradient. Then, the
299 seasonal variations of the biogeochemical properties ($Chla$ and b_{bp}) at the SCM level were
300 studied in relation to environmental conditions. This ultimately led us to identify and
301 describe the main types of SCMs in the five considered regions of the Med Sea.

302 3.1.1 Variability of the SCM along the west-to-east gradient

303 The well-known west-to-east trophic gradient of the Mediterranean was observed in
304 the present dataset, with a decrease in the surface $Chla$ from the NW region (median value of
305 0.15 mg m^{-3}) to the LEV region (median value of 0.04 mg m^{-3} ; Figure 3a). A decrease in the
306 amplitude of the SCM paralleled the surface gradient, with decreasing mean $Chla$ and b_{bp}
307 values in the SCM from the NW to the LEV (0.45 to 0.24 mg m^{-3} and 0.00088 to 0.00050 m^{-1}
308 for $Chla$ and b_{bp} , respectively) (Figures 3b-c). In the Eastern Basin (*i.e.* ION and LEV), only
309 27% of the $Chla$ values were distributed above the median value calculated for the entire
310 Mediterranean Basin (0.28 mg m^{-3}) whereas 66% of the $Chla$ values exceeded it in the
311 Western Basin (*i.e.* NW, SW, and TYR; Figure 4). Similarly, in the Eastern Basin, only ~30%
312 of the b_{bp} values exceeded the median value calculated for the entire Mediterranean Sea in the
313 SCM (0.00058 m^{-1}) (*i.e.* 32% and 29% for the ION and LEV, respectively; Figures 4d-e)
314 whereas in the Western Basin, ~75% of the b_{bp} values were distributed above the global
315 median value (*i.e.* 81%, 80% and 71% for the NW, SW and TYR, respectively, Figures 4a-c).



316 In parallel, from the NW to the LEV regions, a deepening of the SCM (median values
317 of 58 and 95 m, respectively; Figure 3d) and an increase in its thickness (median values of 43
318 and 72 m, respectively; Figure 3e) was observed. A statistical Wilcoxon test revealed non-
319 identical distributions of the considered variables (SCM amplitude, depth and thickness)
320 among the different Mediterranean regions (significance level $p < 0.001$). Our results suggest
321 that the well-known west-to-east trophic gradient of the Mediterranean occurs not only at the
322 surface but also at depth. As suggested by previous studies (Mignot et al., 2014; Lavigne et
323 al., 2015), we confirm that the thickness and depth of the SCM are inversely related to its
324 amplitude. The eastward weakening, deepening and increase in the thickness of the SCM is
325 gradual across the Mediterranean Sea.

326 **3.1.2 Seasonal variations of Chl a and b_{bp}**

327 The seasonal cycle of the Chl a in the SCM was more pronounced in the Western
328 Basin than in the Eastern Basin. This was especially true for the NW (Figure 4a) with median
329 values of Chl a reaching $\sim 0.8 \text{ mg m}^{-3}$ in June-July and $\sim 0.3 \text{ mg m}^{-3}$ in January-February.
330 Similarly, the seasonal cycle of b_{bp} in the SCM was more pronounced in the occidental part of
331 the Med Sea than in the oriental part. Depending on the region and period of the year, the
332 Chl a and b_{bp} values showed synchronous or decoupled seasonal cycles. In the Western Basin,
333 the b_{bp} and Chl a seasonal cycles were coupled. The NW and TYR regions of the Western
334 Basin showed a seasonal cycle characterized by two Chl a peaks at the SCM in March-April
335 and June-July (the SW region presents a single maximum from April to July) and a
336 simultaneous increase in b_{bp} recorded in April-June (Figures 4a-c). On the opposite, the ION
337 and the LEV presented a unique maximum of Chl a in June that is delayed compared to the b_{bp}
338 seasonal maximum occurring in February-April (Figures 4d-e).



339 The chlorophyll *a* concentration is the most commonly used, yet imperfect, indicator of
340 the phytoplankton biomass (Cleveland et al., 1989; Geider, 1993). Variations in Chl*a* may
341 reflect changes in either phytoplankton carbon (Furuya, 1990; Hodges and Rudnick, 2004;
342 Beckmann and Hense, 2007) or in intracellular content as a result of physiological processes
343 occurring in phytoplankton cells, photoacclimation in particular (Geider et al., 1997; Fennel
344 and Boss, 2003). The particulate backscattering coefficient is considered as a proxy of the
345 abundance of particles (Morel and Ahn, 1991; Stramski and Kiefer, 1991; Loisel and Morel,
346 1998; Stramski et al., 2004) and of the stock of Particulate Organic Carbon (POC) in the open
347 ocean waters (Stramski et al., 1999; Balch et al., 2001; Cetinić et al., 2012; Dall’Olmo and
348 Mork, 2014). In contrast with Chl*a*, it provides information on the whole pool of particles, not
349 specifically on phototrophic organisms. The backscattering coefficient also depends on
350 several parameters such as the size distribution, nature, shape, structure and refractive index
351 of the particles (Morel and Bricaud, 1986; Babin and Morel, 2003; Huot et al., 2007b;
352 Whitmire et al., 2010).

353 The vertical and seasonal coupling of Chl*a* and b_{bp} has been shown to reflect an actual
354 increase in carbon biomass whereas a decoupling could result from photoacclimation or from
355 a change in the nature or size distribution of the particle assemblage (Behrenfeld et al., 2005;
356 Flory et al., 2004; Siegel et al., 2005). The results presented above indicate that the Western
357 Basin presents higher values of Chl*a* and b_{bp} in the SCM compared to the Eastern Basin and
358 displays a coupling of the properties all year long (Figure 4). Hence, we suggest that in the
359 NW, SW and TYR regions, the SCM sustains larger phytoplankton carbon biomass than in
360 the ION and LEV regions. Furthermore, in this Eastern part of the Med Sea, the SCM results,
361 at first order, from physiological acclimation to low light and/or from a modification of the
362 nature of the particle assemblage. In the next section, we will analyse the environmental



363 conditions occurring at the SCM level and attempt to determine the factors underpinning the
364 seasonal occurrence of SCMs in the different regions.

365 **3.1.3 Environmental factors controlling the SCM**

366 From a bottom-up perspective, it is the balance between light and nutrient limitations
367 that influences the establishment of phytoplankton communities at depth (Kiefer et al., 1976;
368 Cullen, 1982; Klausmeier and Litchman, 2001; Ryabov, 2012; Latasa et al., 2016). To explore
369 the light-nutrient regime in the SCM, a monthly climatology of the isolume and nitracline in
370 the different considered regions was represented with the depth of the Subsurface Chl a and
371 b_{bp} Maxima (*i.e.* SCM and $Sb_{bp}M$, respectively; Figure 5).

372 In the Western Basin, the isolume $0.3 \text{ mol quanta m}^{-2} \text{ d}^{-1}$, the nitracline $1 \text{ } \mu\text{mol}$, the
373 $Sb_{bp}M$ and the SCM were all located at a similar depth during the oligotrophic period
374 (maximum depth difference $< 20 \text{ m}$; Figures 5a-c). Hence, this part of the Med Sea benefits
375 from both light and nutrient resources and presents an actual increase in phytoplankton
376 biomass (Figures 5 and 6a-b). The shallowest nitracline (median of 61 m ; Figure 6c) and the
377 steepest nitracline (slope of $90 \text{ } \mu\text{mol m}^{-4}$; Figure 6d) were here recorded for the NW, which
378 may indicate higher upward diffusive flux of nitrates available to sustain phytoplankton
379 biomass.

380 In contrast, in the ION and LEV regions, the isolume $0.3 \text{ mol quanta m}^{-2} \text{ d}^{-1}$, nitracline 1
381 μmol , SCM and $Sb_{bp}M$ were not collocated in the water column (Figures 5d-e). The
382 difference between the depths of the SCM and nitracline was $\sim 50 \text{ m}$ during the stratified
383 period (Figures 5d-e and 6a) and the $Sb_{bp}M$ was shallower than the SCM (by $\sim 40 \text{ m}$),
384 suggesting no accumulation of carbon at the SCM. In the Eastern Basin, the nitracline was
385 deeper ($\sim 120 \text{ m}$ in Eastern Basin versus $\sim 70 \text{ m}$ in Western Basin; Figure 6c) and the nutrient
386 gradient was less sharp (nitracline slope of $\sim 40 \text{ } \mu\text{mol m}^{-4}$ in Eastern Basin versus $\sim 90 \text{ } \mu\text{mol m}^{-4}$



387 ⁴ in Western Basin; Figure 6d) than in the Western Basin, suggesting a weak upward diffusive
388 flux of nitrates that corroborates previous results (Tanhua et al., 2013; Pasqueron de
389 Fommervault et al., 2015b). The inverse relationship between the nitracline steepness and the
390 thickness of the SCM is also confirmed (Gong et al., 2017). The PAR at the SCM level was
391 significantly lower in this Eastern part than in the Western part of the Med Sea (Wilcoxon test
392 at a significance level of $p < 0.001$; Figure 6b). The development of the SCM in this system
393 is, thus, limited by both the availability of light and nutrients. The SCM still settles at a depth
394 where light is available at a sufficient level to sustain photosynthesis, but never reaches the
395 nitracline.

396 **3.1.4 Coupling and decoupling of b_{bp} and Chl a in the SCM**

397 From the previous section, we have seen that the SCM of the Western Basin benefits
398 from both light and nutrient resources. In these conditions, the observed simultaneous
399 increase in Chl a and b_{bp} at the SCM most likely represents an actual development of
400 phytoplankton biomass, as indicated by the concordance between the depths of the SCM and
401 the $S_{b_{bp}M}$ (Figure 5). On the opposite, in the Eastern part of the Mediterranean, there is a
402 decoupling of Chl a and b_{bp} in the SCM, the maxima of Chl a and b_{bp} are not co-located. This
403 result suggests that environmental conditions, typically the light conditions, might inhibit the
404 increase in phytoplankton biomass. The microorganisms are, most probably, acclimated or
405 even adapted to these conditions. SCM species are indeed known to use different strategies
406 such as photoacclimation to low light (*i.e.* increase in the intracellular pigment content),
407 mixotrophy or small-scale directed movements towards light (Falkowski and Laroche, 1991;
408 Geider et al., 1997; Clegg et al., 2012). A vertical shift toward species more adapted to the
409 particular environmental conditions prevailing in the SCM layer is a well-known phenomenon
410 (*e.g.* Pollehne et al., 1993; Latasa et al., 2016). For example, two ecotypes of
411 *Prochlorococcus*, characterized by different accessory pigment contents, are known to be



412 adapted to either low-light or high-light conditions and to occupy different niches in the water
413 column (Bouman et al., 2006; Garczarek et al., 2007; Moore and Chisholm, 1999). In
414 particular, the low-light ecotype, characterized by increased intracellular pigmentation, has
415 been frequently observed at the SCM level in the Mediterranean, especially in the oriental
416 part (Brunet et al., 2006; Siokou-Frangou et al., 2010). A west-to-east modification in the
417 composition of phytoplankton communities in the SCM toward a dominance of
418 picophytoplankton species adapted to recurring light limitation, has been observed (Christaki,
419 2001; Crombet et al., 2011; Siokou-Frangou et al., 2010).

420 Whereas photoacclimation is defined as a short-term acclimation of a photosynthetic
421 organism to changing irradiance, photoadaptation refers to the long-term evolutionary
422 adaptation of photosynthetic organisms to ambient light conditions, through genetic selection.
423 Both phenomena could explain the vertical decoupling of b_{bp} and $Chl a$ we observed in the
424 Eastern Basin. Yet our dataset did not allow us to conclude on the dominance of one process
425 compared to the other.

426 Although photoacclimation seems to be a prevalent hypothesis in numerous studies to
427 explain the vertical decoupling of $Chl a$ and b_{bp} (e.g. Brunet et al., 2006; Cullen, 1982; Mignot
428 et al., 2014), it should yet be reminded that this decoupling could also result from a change in
429 the nature or size distribution of the particle assemblage. Small particles are, for example,
430 known to backscatter light more efficiently than large particles (Morel and Bricaud, 1986;
431 Stramski et al., 2004). A higher proportion of nonalgal particles in the Eastern compared to
432 the Western Basin could thus explain the decoupling between b_{bp} and $Chl a$. The nonalgal
433 particles compartment is defined as the background of submicronic living biological cells (*i.e.*
434 viruses or bacteria) and non-living particles (*i.e.* detritus or inorganic particles) and is
435 typically known to represent a significant part of the particulate assemblage in oligotrophic
436 ecosystems (Claustre et al., 1999; Morel and Ahn, 1991; Stramski et al., 2001).



437 **3.2 Classification of the Chl a and b_{bp} vertical profiles**

438 In the previous section, we identified the major environmental factors leading to the
439 occurrence of two main types of SCMs in the five considered regions of the Med Sea. While a
440 concomitant maximum of Chl a and b_{bp} suggested a carbon biomass maximum, a decoupling
441 between the vertical distributions of these two properties may reflect photoacclimation, a
442 modification of the algal community composition, or a change in the nature and/or size of the
443 particle assemblage. The seasonal and regional variability in this global picture of the SCM
444 was explored using a statistical approach applied to the BGC-Argo dataset. Our aim was here
445 to classify the Chl a and b_{bp} profiles based on their shape. This led us to propose a typology
446 of the different types of SCMs seasonally encountered in the five regions of the
447 Mediterranean Sea. It also permitted to assess the frequency of these different types of SCMs
448 over the seasonal cycle and compare their characteristics among the various regions of the
449 Mediterranean Sea.

450 **3.2.1 The NW: a region with a specific trophic regime**

451 In the NW, the vertical distributions of Chl a and b_{bp} presented four different shapes
452 over the annual cycle (Figures 7a-b). The *mixed* shape was characterized by an homogeneous
453 distribution of Chl a and b_{bp} and showed occurrence exceeding 60% from December to March
454 (Figure 8a). The *bloom* shape exhibited high Chl a and b_{bp} values at surface with maximum
455 occurrence > 55% in April. The coexistence of the *mixed* and the *bloom* shapes during winter
456 and spring could result from intermittent mixing that alters the vertical distribution of Chl a
457 and b_{bp} (e.g. Chiswell, 2011; Lacour et al., 2017). The SBM_{aZeu} and the SBM_{bZeu} (SBM
458 occurring above and below the euphotic depth, respectively) constituted two different cases of
459 subsurface maximum. In both cases, Chl a and b_{bp} covaried (Figures 7a-b), the maxima of



460 Chl a and b_{bp} were observed at nearly the same depth suggesting an increase in carbon
461 biomass in subsurface.

462 The SBM_{aZeu} was often observed in late spring and late summer whereas the SBM_{bZeu}
463 occurred more frequently ($> 50\%$) in the middle of the oligotrophic period. This results
464 suggests a deepening of the SCM along the oligotrophic season and corroborates the “light-
465 driven hypothesis” previously formulated by Letelier et al. (2004) and Mignot et al. (2014). In
466 the NW region, the high surface Chl a of the *bloom* shape (Figure 7a) probably results in
467 increased light attenuation in the water column from fall to spring. Consequently, the SCM
468 established shallower in spring than in summer (Figure 5a) and the SBM_{aZeu} shape occurred
469 relatively frequently in spring (Figure 8a). Then, from spring to summer, the Chl a decrease in
470 the surface layer of the water column resulted in decreased light attenuation and subsequent
471 deepening of the SCM (Figure 5a), which thus formed a subsurface maximum of Chl a and b_{bp}
472 below the euphotic layer (SBM_{bZeu} , Figure 8a). Therefore, our results are consistent with
473 previous studies (e.g. Gutiérrez-Rodríguez et al., 2010; Mayot et al., 2017b) that highlighted
474 the special status of the Northwestern region, the only region to exhibit the *bloom* shape and
475 predominantly SBMs during the oligotrophic season (Figures 9a-b).

476 3.2.2 The SW and the TYR: regions of transition

477 In the Southwestern region as well as in the Tyrrhenian Sea, three shapes characterized
478 the seasonal variability of the vertical distribution of Chl a and b_{bp} (Figures 7c-d and e-f). A
479 *mixed* shape, similar to that observed in the NW (Figures 9c-d), a *SBM* shape (Figures 9e-f),
480 and a *SCM* shape (decoupling between the maximum of Chl a and b_{bp} at depth) were
481 successively encountered over the seasonal cycle, with weak differences in their frequency of
482 occurrence among the two regions. The *SCM* shape established shallower in the water column
483 than the *SBM* shape (Figures 7c-f). It was encountered mainly in winter and fall (~50% of



484 occurrence), alternating with the *mixed* shape (Figures 8b-c). Thus, this shape probably
485 illustrates the erosion of the SCM by the winter mixing as previously suggested, for example,
486 in Lavigne et al. (2015). The *SBM* shape occurred mainly during spring and summer (>75%)
487 when both light and nutrients were available for phytoplankton growth (Figures 5b-c). The
488 *SBM* shapes of the SW and the TYR were comparable to the *SBM_{bZeu}* shape of the NW
489 occurring at almost the same depth ($\sim Z_{eu}$). The *SCM* shapes of the SW and TYR were
490 analogous to the *SCM_{aZeu}* shape of the ION and LEV (Figures 9e-h). Hence, our results
491 suggest that the SW and TYR regions are transition regimes that present types of SCMs that
492 can be found in both the Western and Eastern Basins.

493 **3.2.3 The ION and the LEV: oligotrophic end-members**

494 In the Ionian Sea, three different shapes were retrieved along the seasonal cycle, *i.e.* the
495 *mixed*, the *SCM_{aZeu}* and the *SCM_{bZeu}* shapes (Figures 7g-h). In this region, the *Chla* maximum
496 was always decorrelated from the b_{bp} maximum that revealed higher values at surface than at
497 depth. In the Levantine Sea, only two distinct shapes were encountered, *i.e.* the *SCM_{aZeu}* and
498 the *SCM_{bZeu}* shapes (Figures 7i-j). The subsurface maximum of *Chla* was never associated
499 with a subsurface maximum of b_{bp} . Such SCMs constituted a permanent pattern with *SCM_{bZeu}*
500 and *SCM_{aZeu}* reaching occurrences of 100% in June-July and > 75% in December-March,
501 respectively (Figures 8d-e). The *SCM_{bZeu}* shape was a particularity of the Eastern Basin. This
502 shape was very similar in the ION and LEV, but very different from the shapes observed in
503 the other regions (Figures 9g-h). This *SCM_{bZeu}* settled below the Z_{eu} that, in such oligotrophic
504 systems, occurs relatively deep in the water column (~ 95 m; Figure 3d). This type of SCM
505 was also very thick (~ 70 m) (Figure 3e) and associated with low values of the nitracline slope
506 (Figure 6d).



507 **3.3 A case study of the Gulf of Lions and Levantine Sea**

508 Both the climatological and statistical approaches proposed in this study allowed us to
509 characterize the SCM dynamics in five regions of the Mediterranean Sea at large spatial
510 (interregional) and temporal (seasonal) scales. In the present section, we focused on the data
511 provided by two BGC-Argo floats that recorded simultaneously bio-optical properties, PAR
512 and nitrate concentration in two distinct regions, representing the two extremes of the
513 Mediterranean trophic gradient. This helped to gain understanding of the dynamics of the
514 SCM at a weekly and regional scale and should give insights in the mechanisms underlying
515 the occurrence of SCMs in these end-member regimes.

516 **3.3.1 Overview of the two contrasted systems**

517 The float WMO 6901512 (fGL) was been deployed in the Gulf of Lions the 11th of
518 April 2013 and recorded data until the 4th of May, 2014 (Figure 10a). The float WMO
519 6901528 (fLS) collected data in the Levantine Sea from May 18, 2013 to May 23, 2015
520 (Figure 10c). The two regions presented very different seasonal Chl*a* distribution. The Gulf of
521 Lions is a typical “temperate-like” system that exhibits a winter period characterized by large
522 MLDs (Millot, 1999; Lavigne et al., 2015) (maximum MLD > 1000 m, Figure 10d). The
523 intense mixing induces a refueling of nutrients (Gačić et al., 2002; D’Ortenzio et al., 2014;
524 Severin et al., 2017), which allows the development of a spring bloom (Marty et al., 2002,
525 2008; Mayot et al., 2017a) as revealed by the high surface Chl*a* from April to May (Figure
526 10b). A subsurface maximum of Chl*a* established from the end of May to mid-November at a
527 depth similar to that of the nitracline $1 \mu\text{M}$ and isolume $0.3 \text{ mol quanta m}^{-2} \text{ d}^{-1}$, and displayed
528 maximum Chl*a* of $\sim 1 \text{ mg m}^{-3}$ in July (Figure 10b).

529 The Levantine Sea behaves, on the opposite, as a “tropical-like” system. Winter mixing
530 was weak (maximum MLD of 125 m; Figure 10d) but still able to erode the SCM as



531 suggested by the small increase in surface Chl a from November to February (Figure 10b).
532 The seasonal MLD deepening almost never reached the nitracline, thus limiting the nitrate
533 supply to the upper layer of the water column (Dugdale and Wilkerson, 1988; Lavigne et al.,
534 2013; Pasqueron de Fommervault et al., 2015a), hence leading to relatively low surface
535 primary production in this area (Bricaud et al., 2002; Krom et al., 1991; Psarra et al., 2000;
536 Siokou-Frangou et al., 2010). The SCM is a permanent feature in this region, settling below
537 the isolume $0.3 \text{ mol quanta m}^{-2} \text{ d}^{-1}$ and far above the nitracline (Figure 10d).

538 3.3.2 Factors limiting the SCM

539 For exploring the limiting factors at the level of the SCM, we used a nutrient-vs-light
540 resource-limitation diagram. This approach employed in biogeochemical modelling (Cloern,
541 1999; Li and Hansell, 2016) exploits simultaneously PAR and $[\text{NO}_3^-]$ data in order to
542 understand which environmental factor limits phytoplankton growth (Figure 11).

543 In the Gulf of Lions, two different types of situations occurred: (1) very low light compared to
544 the maximum surface PAR ($\text{PAR}_{\text{norm}} < 0.025$) coupled with $\text{NO}_3^-_{\text{norm}}$ comprised between 0
545 and 1, indicative of light limitation; and (2) low light compared to the maximum surface PAR
546 (PAR_{norm} within the range 0.025-0.15) associated with $\text{NO}_3^-_{\text{norm}} < 0.15$, indicative of nitrate
547 limitation, probably resulting from uptake by phytoplankton (Figure 11a). On the contrary, in
548 the Eastern part of the Med Sea, the SCM was always associated with very low light
549 conditions compared to the maximum surface PAR ($\text{PAR}_{\text{norm}} < 0.025$) and variable $\text{NO}_3^-_{\text{norm}}$
550 values comprised between 0.1 and 1 (Figure 11b). This suggests that, even when the nitrate
551 concentration is sufficient to sustain primary production at the SCM level, another factor
552 limits phytoplankton growth. Phytoplankton growth at the SCM is probably limited by light
553 or co-limited by both light and nutrients. Phosphate is also an important limiting factor for
554 phytoplankton growth in the entire Mediterranean Sea (Marty et al., 2002; Pujo-Pay et al.,



555 2011), the Eastern Basin in particular (Krom et al., 1991, 2010). Hence, in a non-nitrate
556 limited SCM of the Levantine (Figure 11b), phytoplankton may still be limited by either or
557 both low phosphate concentrations and low light levels. Since autonomous measurements of
558 phosphate concentrations are not possible yet, our chemical data are restricted to nitrate so we
559 cannot conclude on the role of phosphate in the settlement of the SCM.

560 The coupling between *Chl a* and b_{bp} was studied using the *Chl a*-to- b_{bp} ratio. In both the
561 Western and Eastern Basins, SCMs with prevailing very low light conditions were
562 accompanied by high values of the *Chl a*-to- b_{bp} ratio ($> 300 \text{ mg m}^{-2}$). In contrast, in the SCM
563 of the Western Basin associated with low values of $\text{NO}_3^-_{\text{norm}}$, the *Chl a*-to- b_{bp} ratio showed
564 values $< 300 \text{ mg m}^{-2}$. This ratio is a proxy of the *Chl a*-to-POC ratio (Behrenfeld et al., 2015;
565 Álvarez et al., 2016; Westberry et al., 2016) and constitutes an optical index of
566 photoacclimation (Behrenfeld et al., 2005; Siegel et al., 2005) or of the phytoplankton
567 communities (Cetinić et al., 2012, 2015). Hence, in both the Western and Eastern Basins, the
568 high values of the *Chl a*-to- b_{bp} ratio occurring in the SCM associated with very low light
569 conditions could be attributed to either photoacclimation of phytoplankton cells to low light
570 intensity. In contrast, in the SCM of the Western Basin where low values of $\text{NO}_3^-_{\text{norm}}$ were
571 reported, the low *Chl a*-to- b_{bp} ratio values could either indicate a higher proportion of detrital
572 particles or an increase in biomass sustained by a specific phytoplankton assemblage
573 dominated by communities of nano- or pico-sized cells, including very small diatoms (e.g.
574 Leblanc et al., 2018).

575 4 CONCLUSIONS

576 The present study is, to our knowledge, the first examining the spatial and temporal
577 variability of Subsurface Chlorophyll *a* Maxima (SCMs) in the Mediterranean Sea using
578 BioGeochemical-Argo profiling floats equipped with both light (PAR) and nitrate ($[\text{NO}_3^-]$)



579 sensors. Our study aims to improve the understanding of the characteristics and dynamics of
580 phytoplankton biomass in the subsurface layer of the Mediterranean Sea. We identified two
581 major mechanisms controlling the occurrence of SCMs, *i.e.* (1) SCMs arising from an actual
582 increase in carbon biomass at depth (or SBMs) and benefiting from both light and nutrient
583 resources; and (2) SCMs that stem from an increase in intracellular chlorophyll *a*
584 concentration as a result of photoacclimation to low light levels. In the temperate-like system
585 of the Western Mediterranean Sea, SBMs are recurrent whereas in the “subtropical-like”
586 system of the Eastern Mediterranean Sea, SCMs are, at a first order, representative of
587 photoacclimation process. Using a statistical classification of vertical profiles of Chl*a* and b_{bp}
588 collected over the entire Mediterranean, we have evidenced different intermediate SCM
589 situations that can be summarized as follows (Figure 12):

- 590 1) The SBM_{aZeu} is a Subsurface Biomass Maximum that settles above the euphotic zone in
591 the Northwestern Mediterranean Sea (NW). It is the thinnest (~40m) and shallowest
592 (~60 m) biomass maximum. It is also the most intense, probably because it benefits
593 from adequate light and nutrient resources.
- 594 2) The SBM_{bZeu} establishes below the euphotic zone in the NW. As well as the $SBMs$ of the
595 Southwestern Mediterranean Sea (SW) and Tyrrhenian Sea (TYR), the SBM_{bZeu} is less
596 intense than the SBM_{aZeu} .
- 597 3) The SCM of the SW and TYR as well as the SCM_{aZeu} (*i.e.* settling above the euphotic
598 depth) of the Ionian (ION) and Levantine (LEV) Seas are not biomass subsurface
599 maxima, but reflect Chl*a* maxima resulting from photoacclimation. Moving from the
600 SW to LEV region, the amplitude of the SCM decreases while its thickness increases.
- 601 4) The SCM_{bZeu} of the ION and LEV settle below the euphotic depth and are deeper (~95
602 m) than all the other subsurface maxima. They represent the oligotrophic end-member
603 type of subsurface maxima in the Med Sea. In these types of SCMs, phytoplankton



604 communities most probably establish deep in the water column, in order to reach the
605 nutrient resources. These communities are likely photoacclimated, and also possibly
606 photoadapted, to the low light conditions encountered at such depths. The
607 phytoplankton assemblage is likely composed of picophytoplankton (Casotti et al.,
608 2003; Siokou-Frangou et al., 2010), including the low-light adapted *Prochlorococcus*
609 ecotype (Brunet et al., 2006; Garczarek et al., 2007).

610 In stratified oligotrophic ecosystems, the SCM phytoplankton species may settle
611 especially deep and adapt to the prevailing low-light levels in order to benefit from more
612 nutrients. On the contrary, when nitrates are not a limiting factor at the SCM level (e.g. in the
613 northwestern region after the bloom period), the SCM is only controlled by the amount of
614 light available at depth. In either case, light is a crucial forcing parameter that controls the
615 depth of the SCM. Consistently with previous studies conducted in other open ocean regions
616 (Longhurst and Glen Harrison, 1989; Furuya, 1990; Severin et al., 2017), the present work
617 suggests that shallower SCMs tend to display larger phytoplankton biomass than deeper
618 SCMs. In our study, these biomass maxima are characterized by a coupling of $Chl a$ and b_{bp}
619 that suggests an increase in carbon biomass. Finally, the present results indicate that SBMs
620 represent a frequent feature in the Med Sea, which contrasts with the idea that SCMs in
621 oligotrophic regions typically result from photoacclimation of phytoplankton cells. Thus, we
622 suggest that the contribution of SCMs to primary production, which may be substantial
623 although ignored by current satellite-based estimates, should be further investigated.

624 **ACKNOWLEDGEMENTS**

625 This paper represents a contribution to the following research projects: remOcean
626 (funded by the European Research Council, grant 246777), NAOS (funded by the Agence
627 Nationale de la Recherche in the frame of the French ‘‘Equipement d’avenir’’ program, grant



628 ANR J11R107-F), the SOCLIM (Southern Ocean and climate) project supported by the
629 French research program LEFE- CYBER of INSU-CNRS, the Climate Initiative of the
630 foundation BNP Paribas and the French polar institute (IPEV), AtlantOS (funded by the
631 European Union’s Horizon 2020 Research and Innovation program, grant 2014– 633211), E-
632 AIMS (funded by the European Commission’s FP7 project, grant 312642), U.K. Bio-Argo
633 (funded by the British Natural Environment Research Council—NERC, grant NE/
634 L012855/1), REOPTIMIZE (funded by the European Union’s Horizon 2020 Research and
635 Innovation program, Marie Skłodowska-Curie grant 706781), Argo-Italy (funded by the
636 Italian Ministry of Education, University and Research - MIUR), and the French Bio-Argo
637 program (BGC-Argo France; funded by CNES-TOSCA, LEFE Cyber, and GMMC). We
638 thank the PIs of several BGC-Argo floats missions and projects: Giorgio Dall’Olmo
639 (Plymouth Marine Laboratory, United Kingdom; E-AIMS and U.K. Bio- Argo); Kjell-Arne
640 Mork (Institute of Marine Research, Norway; E-AIMS); Violeta Slabakova (Bulgarian
641 Academy of Sciences, Bulgaria; E-AIMS); Emil Stanev (University of Oldenburg, Germany;
642 E-AIMS); Claire Lo Monaco (Laboratoire d’Océanographie et du Climat: Expérimentations et
643 Approches Numériques); Pierre-Marie Poulain (National Institute of Oceanography and
644 Experimental Geophysics, Italy; Argo- Italy); Sabrina Speich (Laboratoire de Météorologie
645 Dynamique, France; LEFE- GMMC); Virginie Thierry (Ifremer, France; LEFE-GMMC);
646 Pascal Conan (Observatoire Océanologique de Banyuls sur mer, France; LEFE-GMMC);
647 Laurent Coppola (Laboratoire d’Océanographie de Villefranche, France; LEFE-GMMC);
648 Anne Petrenko (Mediterranean Institute of Oceanography, France; LEFE-GMMC); and Jean-
649 Baptiste Sallée (Laboratoire d’Océanographie et du Climat, France; LEFE-GMMC). Louis
650 Prieur and Jean-Olivier Irisson (Laboratoire d’Océanographie de Villefranche, France) are
651 acknowledged for useful comments and fruitful discussion. We also thank the International



652 Argo Program and the CORIOLIS project that contribute to make the data freely and publicly
653 available.

654 REFERENCES

655 Álvarez, E., Morán, X. A. G., López-Urrutia, Á. and Nogueira, E.: Size-dependent photoacclimation of the
656 phytoplankton community in temperate shelf waters (southern Bay of Biscay), *Marine Ecology Progress Series*, 543, 73–87,
657 doi:10.3354/meps11580, 2016.

658 Anderson, G. C.: Subsurface Chlorophyll Maximum in the Northeast Pacific Ocean, *Limnology and Oceanography*,
659 14(3), 386–391, 1969.

660 Antoine, D., Morel, A. and André, J.-M.: Algal pigment distribution and primary production in the eastern
661 Mediterranean as derived from coastal zone color scanner observations, *Journal of Geophysical Research*, 100, 16193–
662 16209, 1995.

663 Arai, R., Nishiyama, N., Nakatani, N. and Okuno, T.: Measurement Method of Nutrient using Principal Component
664 Regression, in *OCEANS 2008-MTS/IEEE Kobe Techno-Ocean, IEEE.*, pp. 1–6., 2008.

665 Ardyna, M., Babin, M., Gosselin, M., Devred, E., Bélanger, S., Matsuoka, A. and Tremblay, J. E.: Parameterization
666 of vertical chlorophyll a in the Arctic Ocean: Impact of the subsurface chlorophyll maximum on regional, seasonal, and
667 annual primary production estimates, *Biogeosciences*, 10(6), 4383–4404, doi:10.5194/bg-10-4383-2013, 2013.

668 Arrigo, K. R., Matrai, P. A. and Van Dijken, G. L.: Primary productivity in the Arctic Ocean: Impacts of complex
669 optical properties and subsurface chlorophyll maxima on large-scale estimates, *Journal of Geophysical Research: Oceans*,
670 116(11), 1–15, doi:10.1029/2011JC007273, 2011.

671 Babin, M., Morel, A., Fournier-Sicre, V., Fell, F. and Stramski, D.: Light scattering properties of marine particles in
672 coastal and open ocean waters as related to the particle mass concentration, *Limnology and Oceanography*, 48(2), 843–859,
673 doi:10.4319/lo.2003.48.2.0843, 2003.

674 Balch, W. M., Drapeau, D. T., Fritz, J. J., Bowler, B. C. and Nolan, J.: Optical backscattering in the Arabian Sea—
675 continuous underway measurements of particulate inorganic and organic carbon, *Deep Sea Research Part I: Oceanographic*
676 *Research Papers*, 48(11), 2423–2452, doi:10.1016/S0967-0637(01)00025-5, 2001.

677 Barbieux, M., Uitz, J., Bricaud, A., Organelli, E., Poteau, A., Schmechtig, C., Gentili, B., Penker, C., Leymarie,
678 E., D'Ortenzio, F. and Claustre, H.: Assessing the Variability in the Relationship Between the Particulate Backscattering
679 Coefficient and the Chlorophyll a Concentration From a Global Biogeochemical-Argo Database, *Journal of Geophysical*



- 680 Research: Oceans, 123(2), 1229–1250, doi:10.1002/2017JC013030, 2018.
- 681 Beckmann, A. and Hense, I.: Beneath the surface: Characteristics of oceanic ecosystems under weak mixing
682 conditions - A theoretical investigation, *Progress in Oceanography*, 75(4), 771–796, doi:10.1016/j.pocean.2007.09.002, 2007.
- 683 Behrenfeld, M. J., Boss, E., Siegel, D. A. and Shea, D. M.: Carbon-based ocean productivity and phytoplankton
684 physiology from space, *Global Biogeochemical Cycles*, 19(1), GB1006, doi:10.1029/2004GB002299, 2005.
- 685 Behrenfeld, M. J., O'Malley, R. T., Boss, E. S., Westberry, T. K., Graff, J. R., Halsey, K. H., Milligan, A. J., Siegel,
686 D. A. and Brown, M. B.: Revaluating ocean warming impacts on global phytoplankton, *Nature Climate Change*, 6(3), 323–
687 330, doi:10.1038/nclimate2838, 2015.
- 688 Bethoux, J. P., Morin, P., Madec, C. and Gentili, B.: Phosphorus and nitrogen behaviour in the Mediterranean Sea,
689 *Deep Sea Research Part A, Oceanographic Research Papers*, 39(9), 1641–1654, doi:10.1016/0198-0149(92)90053-V, 1992.
- 690 Bosc, E., Bricaud, A. and Antoine, D.: Seasonal and interannual variability in algal biomass and primary production
691 in the Mediterranean Sea, as derived from 4 years of SeaWiFS observations, *Global Biogeochemical Cycles*, 18(GB1005),
692 doi:10.1029/2003GB002034, 2004.
- 693 Bouman, H., Ulloa, O., Scanlan, D. J., Zwirgmaier, K., Li, W. K. W., Platt, T., Stuart, V., Barlow, R., Leth, O.,
694 Clementson, L., Lutz, V. A., Fukasawa, M., Watanabe, S. and Sathyendranath, S.: Oceanographic Basis of the Global
695 Surface Distribution of *Prochlorococcus* Ecotypes, *Science*, 312(5775), 918–921, doi:10.1126/science.39.1002.398, 2006.
- 696 de Boyer Montégut, C.: Mixed layer depth over the global ocean: An examination of profile data and a profile-based
697 climatology, *Journal of Geophysical Research*, 109(C12), 1–20, doi:10.1029/2004JC002378, 2004.
- 698 Bricaud, A., Bosc, E. and Antoine, D.: Algal biomass and sea surface temperature in the Mediterranean Basin
699 Intercomparison of data from various satellite sensors, and implications for primary production estimates, *Remote Sensing of*
700 *Environment*, 81(2–3), 163–178, 2002.
- 701 Briggs, N., Perry, M. J., Cetinić, I., Lee, C., D'Asaro, E., Gray, A. M. and Rehm, E.: High-resolution observations of
702 aggregate flux during a sub-polar North Atlantic spring bloom, *Deep Sea Research Part I: Oceanographic Research Papers*,
703 58(10), 1031–1039, doi:10.1016/j.dsr.2011.07.007, 2011.
- 704 Brunet, C., Casotti, R., Vantrepotte, V., Corato, F. and Conversano, F.: Picophytoplankton diversity and
705 photoacclimation in the Strait of Sicily (Mediterranean Sea) in summer. I. Mesoscale variations, *Aquatic Microbial Ecology*,
706 44(2), 127–141, doi:10.3354/ame044127, 2006.
- 707 Casotti, R., Landolfi, A., Brunet, C., D'Ortenzio, F., Mangoni, O. and Ribera d'Alcalá, M.: Composition and
708 dynamics of the phytoplankton of the Ionian Sea (eastern Mediterranean), *Journal of Geophysical Research*, 108(C9), 8116,
709 doi:10.1029/2002JC001541, 2003.



- 710 Cetinić, I., Perry, M. J., Briggs, N. T., Kallin, E., D'Asaro, E. A. and Lee, C. M.: Particulate organic carbon and
711 inherent optical properties during 2008 North Atlantic Bloom Experiment, *Journal of Geophysical Research*, 117(C6),
712 doi:10.1029/2011JC007771, 2012.
- 713 Cetinić, I., Perry, M. J., D'Asaro, E., Briggs, N., Poulton, N., Sieracki, M. E. and Lee, C. M.: A simple optical index
714 shows spatial and temporal heterogeneity in phytoplankton community composition during the 2008 North Atlantic Bloom
715 Experiment, *Biogeosciences*, 12(7), 2179–2194, doi:10.5194/bg-12-2179-2015, 2015.
- 716 Chiswell, S. M.: Annual cycles and spring blooms in phytoplankton: Don't abandon Sverdrup completely, *Marine
717 Ecology Progress Series*, 443, 39–50, doi:10.3354/meps09453, 2011.
- 718 Christaki, U.: Nanoflagellate predation on auto- and heterotrophic picoplankton in the oligotrophic Mediterranean
719 Sea, *Journal of Plankton Research*, 23(11), 1297–1310, doi:10.1093/plankt/23.11.1297, 2001.
- 720 Claustre, H., Morel, A., Babin, M., Cailliau, C., Marie, D., Marty, J.-C., Tailliez, D. and Vaultot, D.: Variability in
721 particle attenuation and chlorophyll fluorescence in the tropical Pacific: Scales, patterns, and biogeochemical implications,
722 *Journal of Geophysical Research*, 104(C2), 3401–3422, 1999.
- 723 Claustre, H., Bishop, J., Boss, E., Bernard, S., Berthon, J.-F., Coatanoan, C., Johnson, K. S., Lotiker, A., Ulloa, O.,
724 Perry, M. J., D'Ortenzio, F., Hembise Fanton D'andon, O. and Uitz, J.: Bio-optical profiling floats as new observational tools
725 for biogeochemical and ecosystem studies: Potential synergies with ocean color remote sensing., in "Proceedings of the
726 OceanObs'09: Sustained Ocean Observations and Information for Society" Conference, edited by J. Hall, D. E. Harrison, and
727 D. Stammer, ESA Publ. WPP-306, Venice, Italy, 21–25 Sep., 2010.
- 728 Clegg, M. R., Gaedke, U., Boehrer, B. and Spijkerman, E.: Complementary ecophysiological strategies combine to
729 facilitate survival in the hostile conditions of a deep chlorophyll maximum, *Oecologia*, 169(3), 609–622,
730 doi:10.1007/s00442-011-2225-4, 2012.
- 731 Cleveland, J. S., Perry, M. J., Kiefer, D. A. and Talbot, M. C.: Maximal quantum yield of photosynthesis in the
732 northwest Sargasso Sea., *Journal of Marine Research*, 47(4), 869–886., 1989.
- 733 Cloern, J. E.: The relative importance of light and nutrient limitation of phytoplankton growth: A simple index of
734 coastal ecosystem sensitivity to nutrient enrichment, *Aquatic Ecology*, 33(1), 3–16, doi:10.1023/A:1009952125558, 1999.
- 735 Crombet, Y., Leblanc, K., Queguiner, B., Moutin, T., Rimmelin, P., Ras, J., Claustre, H., Leblond, N., Oriol, L. and
736 Pujo-Pay, M.: Deep silicon maxima in the stratified oligotrophic Mediterranean Sea, *Biogeosciences*, 8(2), 459–475,
737 doi:10.5194/bg-8-459-2011, 2011.
- 738 Cullen, J. J.: The Deep Chlorophyll Maximum: Comparing Vertical Profiles of Chlorophyll a, *Canadian Journal of
739 Fisheries and Aquatic Sciences*, 39(5), 791–803, doi:10.1139/f82-108, 1982.
- 740 Cullen, J. J. and Eppley, R. W.: Chlorophyll Maximum Layers of the Southern-California Bight and Possible



- 741 Mechanisms of their Formation and Maintenance, *Oceanologica Acta*, 4(1), 23–32, 1981.
- 742 D’Ortenzio, F. and D’Alcalá, M. R.: On the trophic regimes of the Mediterranean Sea: A satellite analysis,
743 *Biogeosciences*, 6(2), 139–148, doi:10.5194/bg-6-139-2009, 2009.
- 744 D’Ortenzio, F., Lavigne, H., Besson, F., Claustre, H., Coppola, L., Garcia, N., Laës-Huon, A., Le Reste, S., Malardé,
745 D., Migon, C., Morin, P., Mortier, L., Poteau, A., Prieur, L., Raimbault, P. and Testor, P.: Observing mixed layer depth,
746 nitrate and chlorophyll concentrations in the northwestern Mediterranean: A combined satellite and NO₃ profiling floats
747 experiment, *Geophysical Research Letters*, 41, 6443–6451, doi:10.1002/2014GL061020, 2014.
- 748 Dall’Olmo, G. and Mork, K. A.: Carbon export by small particles in the Norwegian Sea, *Geophysical Research*
749 *Letters*, 41(8), 2921–2927, doi:10.1002/2014GL059244, 2014.
- 750 Dubinsky, Z. and Stambler, N.: Photoacclimation processes in phytoplankton: Mechanisms, consequences, and
751 applications, *Aquatic Microbial Ecology*, 56(2–3), 163–176, doi:10.3354/ame01345, 2009.
- 752 Dugdale, R. C. and Wilkerson, F. P.: Nutrient sources and primary production in the Eastern Mediterranean, in
753 *Océanographie pélagique méditerranéenne*, edited by H. J. Minas and P. Nival, pp. 179–184., 1988.
- 754 Estrada, M., Marrasé, C., Latasa, M., Berdalet, E., Delgado, M. and Riera, T.: Variability of deep chlorophyll
755 maximum in the Northwestern Mediterranean, *Marine Ecology Progress Series*, 92, 289–300, doi:10.3354/meps092289,
756 1993.
- 757 Falkowski, P. G. and Laroche, J.: Acclimation to spectral irradiance in algae, *Journal of Phycology*, 27(1), 8–14,
758 doi:10.1111/j.0022-3646.1991.00008.x, 1991.
- 759 Fasham, M. J. R., Platt, T., Irwin, B. and Jones, K.: Factors affecting the spatial pattern of the deep chlorophyll
760 maximum in the region of the Azores front, *Progress in Oceanography*, 14(C), 129–165, doi:10.1016/0079-6611(85)90009-6,
761 1985.
- 762 Fennel, K. and Boss, E.: Subsurface maxima of phytoplankton and chlorophyll: Steady-state solutions from a simple
763 model, *Limnology and Oceanography*, 48(4), 1521–1534, doi:10.4319/lo.2003.48.4.1521, 2003.
- 764 Flory, E. N., Hill, P. S., Milligan, T. G. and Grant, J.: The relationship between flocculation area and backscatter during a
765 spring phytoplankton bloom, *Deep Sea Research Part I: Oceanographic Research Papers*, 51(2), 213–223,
766 doi:10.1016/j.dsr.2003.09.012, 2004.
- 767 Furuya, K.: Subsurface chlorophyll maximum in the tropical and subtropical western Pacific Ocean: Vertical profiles
768 of phytoplankton biomass and its relationship with chlorophyll a and particulate organic carbon, *Marine Biology*, 107, 529–
769 539, doi:10.1007/bf01313438, 1990.
- 770 Gačić, M., Civitarese, G., Miserocchi, S., Cardin, V., Crise, A. and Mauri, E.: The open-ocean convection in the



- 771 Southern Adriatic: A controlling mechanism of the spring phytoplankton bloom, *Continental Shelf Research*, 22(14), 1897–
772 1908, doi:10.1016/S0278-4343(02)00050-X, 2002.
- 773 Garczarek, L., Dufresne, A., Rousvoal, S., West, N. J., Mazard, S., Marie, D., Claustre, H., Raimbault, P., Post, A. F.,
774 Scanlan, D. J. and Partensky, F.: High vertical and low horizontal diversity of *Prochlorococcus* ecotypes in the Mediterranean
775 Sea in summer, *FEMS Microbiology Ecology*, 60(2), 189–206, doi:10.1111/j.1574-6941.2007.00297.x, 2007.
- 776 Gardner, W. D., Richardson, M. J. and Smith, W. O.: Seasonal patterns of water column particulate organic carbon
777 and fluxes in the Ross Sea, Antarctica, *Deep Sea Research Part II: Topical Studies in Oceanography*, 47, 3423–3449,
778 doi:10.1016/S0967-0645(00)00074-6, 2000.
- 779 Geider, R. J.: Quantitative phytoplankton physiology: implications for primary production and phytoplankton growth,
780 *ICES Marine Science Symposium*, 197, 52–62, 1993.
- 781 Geider, R. J., MacIntyre, H. L. and Kana, T. M.: Dynamic model of phytoplankton growth and acclimation:
782 Responses of the balanced growth rate and the chlorophyll a:carbon ratio to light, nutrient-limitation and temperature, *Marine*
783 *Ecology Progress Series*, 148(1–3), 187–200, doi:10.3354/meps148187, 1997.
- 784 Golub, G. H. and Van Loan, C. F.: *Matrix Computations*, The Johns., Baltimore and London., 1996.
- 785 Gong, X., Jiang, W., Wang, L., Gao, H., Boss, E., Yao, X., Kao, S. J. and Shi, J.: Analytical solution of the nitracline
786 with the evolution of subsurface chlorophyll maximum in stratified water columns, *Biogeosciences*, 14(9), 2371–2386,
787 doi:10.5194/bg-14-2371-2017, 2017.
- 788 Gordon, H. R. and McCluney, W. R.: Estimation of the Depth of Sunlight Penetration in the Sea for Remote Sensing,
789 *Applied Optics*, 14(2), 413–416, doi:10.1364/AO.14.000413, 1975.
- 790 Gutiérrez-Rodríguez, A., Latasa, M., Estrada, M., Vidal, M. and Marrasé, C.: Carbon fluxes through major
791 phytoplankton groups during the spring bloom and post-bloom in the Northwestern Mediterranean Sea, *Deep Sea Research*
792 *Part I: Oceanographic Research Papers*, 57(4), 486–500, doi:10.1016/j.dsr.2009.12.013, 2010.
- 793 Hodges, B. A. and Rudnick, D. L.: Simple models of steady deep maxima in chlorophyll and biomass, *Deep-Sea*
794 *Research Part I: Oceanographic Research Papers*, 51(8), 999–1015, doi:10.1016/j.dsr.2004.02.009, 2004.
- 795 Holm-Hansen, O. and Hewes, C. D.: Deep chlorophyll-a maxima (DCMs) in Antarctic waters: I. Relationships
796 between DCMs and the physical, chemical, and optical conditions in the upper water column, *Polar Biology*, 27(11), 699–
797 710, doi:10.1007/s00300-004-0641-1, 2004.
- 798 Huot, Y., Babin, M., Bruyant, F., Grob, C., Twardowski, M. S., Claustre, H. and To, C.: Relationship between
799 photosynthetic parameters and different proxies of phytoplankton biomass in the subtropical ocean, *Biogeosciences*, 4(5),
800 853–868, doi:10.5194/bg-4-853-2007, 2007.



- 801 Ignatiades, L., Psarra, S., Zervakis, V., Pagou, K., Souvermezoglou, E., Assimakopoulou, G. and Gotsis-Skretas, O.:
802 Phytoplankton size-based dynamics in the Aegean Sea (Eastern Mediterranean), *Journal of Marine Systems*, 36(1–2), 11–28,
803 doi:10.1016/S0924-7963(02)00132-X, 2002.
- 804 Johnson, K. and Claustre, H.: Bringing Biogeochemistry into the Argo Age, *Eos*, 1–7, doi:10.1029/2016EO062427,
805 2016.
- 806 Johnson, K., Berelson, W., Boss, E., Chase, Z., Claustre, H., Emerson, S., Gruber, N., Körtzinger, A., Perry, M. J.
807 and Riser, S.: Observing Biogeochemical Cycles at Global Scales with Profiling Floats and Gliders: Prospects for a Global
808 Array, *Oceanography*, 22(3), 216–225, doi:10.5670/oceanog.2009.81, 2009.
- 809 Johnson, K. S. and Coletti, L. J.: In situ ultraviolet spectrophotometry for high resolution and long-term monitoring
810 of nitrate, bromide and bisulfide in the ocean, *Deep-Sea Research Part I: Oceanographic Research Papers*, 49(7), 1291–1305,
811 doi:10.1016/S0967-0637(02)00020-1, 2002.
- 812 Johnson, K. S., Plant, J. N., Coletti, L. J., Jannasch, H. W., Sakamoto, C. M., Riser, S. C., Swift, D. D., Williams, N.
813 L., Boss, E., Haëntjens, N., Talley, L. D. and Sarmiento, J. L.: Biogeochemical sensor performance in the SOCCOM
814 profiling float array, *Journal of Geophysical Research: Oceans*, 122(8), 6416–6436, doi:10.1002/2017JC012838, 2017.
- 815 Kiefer, D. A., Olson, R. J. and Holm-Hansen, O.: Another look at the nitrite and chlorophyll maxima in the central
816 North Pacific, *Deep-Sea Research and Oceanographic Abstracts*, 23(12), 1199–1208, doi:10.1016/0011-7471(76)90895-0,
817 1976.
- 818 Kimor, B., Berman, T. and Schneller, A.: Phytoplankton assemblages in the deep chlorophyll maximum layers off the
819 Mediterranean coast of Israel, *Journal of Plankton Research*, 34(11), 433–443, doi:10.1016/0198-0254(87)90913-7, 1987.
- 820 Klausmeier, C. a. and Litchman, E.: Algal games: The vertical distribution of phytoplankton in poorly mixed water
821 columns, *Limnology and Oceanography*, 46(8), 1998–2007, doi:10.4319/lo.2001.46.8.1998, 2001.
- 822 Krom, M. D., Kress, N., Brenner, S. and Gordon, L. I.: Phosphorus Limitation of Primary Productivity in the Eastern
823 Mediterranean-Sea, *Limnology and Oceanography*, 36(3), 424–432, doi:10.4319/lo.1991.36.3.0424, 1991.
- 824 Krom, M. D., Emeis, K. C. and Van Cappellen, P.: Why is the Eastern Mediterranean phosphorus limited?, *Progress*
825 *in Oceanography*, 85(3–4), 236–244, doi:10.1016/j.pocean.2010.03.003, 2010.
- 826 Lacour, L., Ardyna, M., Stec, K. F., Claustre, H., Prieur, L., Poteau, A., Ribera D’Alcala, M. and Iudicone, D.:
827 Unexpected winter phytoplankton blooms in the North Atlantic subpolar gyre, *Nature Geoscience*, 10(11), 836–839,
828 doi:10.1038/NGEO3035, 2017.
- 829 Latasa, M., Gutiérrez-rodríguez, A., Cabello, A. M. and Scharek, R.: Influence of light and nutrients on the vertical
830 distribution of marine phytoplankton groups in the deep chlorophyll maximum, *Planet Ocean*, 80(S1), 57–62,
831 doi:10.3989/scimar.04316.01A, 2016.



- 832 Lavigne, H., D'Ortenzio, F., Migon, C., Claustre, H., Testor, P., D'Alcalà, M. R., Lavezza, R., Houpert, L. and
833 Prieur, L.: Enhancing the comprehension of mixed layer depth control on the Mediterranean phytoplankton phenology,
834 *Journal of Geophysical Research: Oceans*, 118(7), 3416–3430, doi:10.1002/jgrc.20251, 2013.
- 835 Lavigne, H., D'Ortenzio, F., Ribera D'Alcalà, M., Claustre, H., Sauzède, R. and Gacic, M.: On the vertical
836 distribution of the chlorophyll a concentration in the Mediterranean Sea: a basin scale and seasonal approach,
837 *Biogeosciences*, 12(5), 4139–4181, doi:10.5194/bg-12-4139-2015, 2015.
- 838 Leblanc, K., Quéguiner, B., Diaz, F., Cornet, V., Michel-Rodriguez, M., Durrieu de Madron, X., Bowler, C.,
839 Malviya, S., Thyssen, M., Grégori, G., Rembauville, M., Grosso, O., Poulain, J., de Vargas, C., Pujo-Pay, M. and Conan, P.:
840 Nanoplanktonic diatoms are globally overlooked but play a role in spring blooms and carbon export, *Nature*
841 *Communications*, 9(1), 953, doi:10.1038/s41467-018-03376-9, 2018.
- 842 Letelier, R. M., Karl, D. M., Abbott, M. R. and Bidigare, R. R.: Light driven seasonal patterns of chlorophyll and
843 nitrate in the lower euphotic zone of the North Pacific Subtropical Gyre, *Limnology and Oceanography*, 49(2), 508–519,
844 doi:10.4319/lo.2004.49.2.0508, 2004.
- 845 Lewis, M. R., Cullen, J. J. and Platt, T.: Phytoplankton and thermal structure in the upper ocean: Consequences of
846 nonuniformity in chlorophyll profile, *Journal of Geophysical Research: Oceans*, 88(C4), 2565–2570,
847 doi:10.1029/JC088iC04p02565, 1983.
- 848 Li, Q. P. and Hansell, D. A.: Mechanisms controlling vertical variability of subsurface chlorophyll maxima in a
849 mode-water eddy, *JOURNAL OF MARINE RESEARCH*, 74(3), 175–199, doi:10.1357/002224016819594827, 2016.
- 850 Loisel, H. and Morel, A.: Light scattering and chlorophyll concentration in case 1 waters: A reexamination,
851 *Limnology and Oceanography*, 43(5), 847–858, doi:10.4319/lo.1998.43.5.0847, 1998.
- 852 Longhurst, A. R. and Glen Harrison, W.: The biological pump: Profiles of plankton production and consumption in
853 the upper ocean, *Progress in Oceanography*, 22(1), 47–123, doi:10.1016/0079-6611(89)90010-4, 1989.
- 854 Marty, J.-C., Garcia, N. and Raimbault, P.: Phytoplankton dynamics and primary production under late summer
855 conditions in the NW Mediterranean Sea, *Deep Sea Research Part I: Oceanographic Research Papers*, 55(9), 1131–1149,
856 doi:10.1016/j.dsr.2008.05.001, 2008.
- 857 Marty, J. C., Chiavérini, J., Pizay, M. D. and Avril, B.: Seasonal and interannual dynamics of nutrients and
858 phytoplankton pigments in the western Mediterranean Sea at the DYFAMED time-series station (1991-1999), *Deep-Sea*
859 *Research Part II: Topical Studies in Oceanography*, 49(11), 1965–1985, doi:10.1016/S0967-0645(02)00022-X, 2002.
- 860 Mayot, N., D'Ortenzio, F., Uitz, J., Gentili, B., Ras, J., Vellucci, V., Golbol, M., Antoine, D. and Claustre, H.:
861 Influence of the phytoplankton community structure on the spring and annual primary production in the North-Western
862 Mediterranean Sea, *Journal of Geophysical Research: Oceans*, 122, doi:10.1002/2016JC012668, 2017a.



- 863 Mayot, N., D’Ortenzio, F., Taillandier, V., Prieur, L., Pasqueron de Fommervault, O., Claustre, H., Bosse, A., Testor,
864 P. and Conan, P.: Physical and biogeochemical controls of the phytoplankton blooms in North-Western Mediterranean Sea:
865 A multiplatform approach over a complete annual cycle (2012-2013 DEWEX experiment), *Journal of Geophysical Research:*
866 *Oceans*, 122, doi:10.1002/2016JC012052, 2017b.
- 867 Mignot, A., Claustre, H., Uitz, J., Poteau, A., D’Ortenzio, F. and Xing, X.: Understanding the seasonal dynamics of
868 phytoplankton biomass and the deep chlorophyll maximum in oligotrophic environments: A Bio-Argo float investigation,
869 *Global Biogeochemical Cycles*, 28(8), 1–21, doi:10.1002/2013GB004781., 2014.
- 870 Mignot, A., Ferrari, R. and Claustre, H.: Floats with bio-optical sensors reveal what processes trigger the North
871 Atlantic bloom, *Nature Communications*, 9(1), 190, doi:10.1038/s41467-017-02143-6, 2018.
- 872 Mikaelyan, A. S. and Belyaeva, G. A.: Chlorophyll “a” content in cells of Antarctic phytoplankton, *Polar Biology*,
873 15(6), 437–445, doi:10.1007/BF00239721, 1995.
- 874 Millot, C.: Circulation in the Western Mediterranean Sea, *Journal of Marine Systems*, 20(1–4), 423–442,
875 doi:10.1016/S0924-7963(98)00078-5, 1999.
- 876 Moore, L. R. and Chisholm, S. W.: Photophysiology of the marine cyanobacterium *Prochlorococcus*: Ecotypic
877 differences among cultured isolates, *Limnology and Oceanography*, 44(3), 628–638, doi:10.4319/lo.1999.44.3.0628, 1999.
- 878 Morel, A. and Ahn, Y.: Optics of heterotrophic nanoflagellates and ciliates: A tentative assessment of their scattering
879 role in oceanic waters compared to those of bacterial and algal cells, *Journal of Marine Research*, 49(1), 177–202, 1991.
- 880 Morel, A. and André, J.-M.: Pigment distribution and Primary Production in the Western Mediterranean as Derived
881 and Modeled From Coastal Zone Color Scanner Observations, *Journal of Geophysical Research*, 96(C7), 12685–12698,
882 doi:10.1029/91JC00788, 1991.
- 883 Morel, A. and Berthon, J.-F.: Surface pigments, algal biomass profiles, and potential production of the euphotic layer:
884 Relationships reinvestigated in view of remote-sensing applications, *Limnology and Oceanography*, 34(8), 1545–1562,
885 doi:10.4319/lo.1989.34.8.1545, 1989.
- 886 Morel, A. and Bricaud, A.: Inherent optical properties of algal cells including picoplankton: theoretical and
887 experimental results, *Canadian Bulletin of Fisheries and Aquatic Science*, 214, 521–559, 1986.
- 888 Morris, A. W. and Riley, J. P.: The determination of nitrate in sea water, *Analytica Chimica Acta*, 29, 272–279,
889 doi:10.1016/S0003-2670(00)88614-6, 1963.
- 890 NREL: SOLPOS 2.0 Documentation. Technical Report, 2000.
- 891 Organelli, E., Claustre, H., Bricaud, A., Schmechtig, C., Poteau, A., Xing, X., Prieur, L., D’Ortenzio, F., Dall’Olmo,
892 G. and Vellucci, V.: A novel near real-time quality-control procedure for radiometric profiles measured by Bio-Argo floats:



- 893 protocols and performances, *Journal of Atmospheric and Oceanic Technology*, 33, 937–951, doi:10.1175/JTECH-D-15-
894 0193.1, 2016.
- 895 Organelli, E., Claustre, H., Bricaud, A., Barbieux, M., Uitz, J., D’Ortenzio, F. and Dall’Olmo, G.: Bio-optical
896 anomalies in the world’s oceans: An investigation on the diffuse attenuation coefficients for downward irradiance derived
897 from Biogeochemical Argo float measurements, *Journal of Geophysical Research: Oceans*, 122, 2017–2033,
898 doi:doi:10.1002/2016JC012629., 2017.
- 899 Parslow, J. S., Boyd, P. W., Rintoul, S. R. and Griffiths, F. B.: A persistent subsurface chlorophyll maximum in the
900 Interpolar Frontal Zone south of Australia: Seasonal progression and implications for phytoplankton-light-nutrient
901 interactions, *Journal of Geophysical Research: Oceans*, 106(C12), 31543–31557, doi:10.1029/2000JC000322, 2001.
- 902 Pasqueron de Fommervault, O., D’Ortenzio, F., Mangin, A., Serra, R., Migon, C., Claustre, H., Lavigne, H., Ribera
903 d’Alcala, M., Prieur, L., Taillandier, V., Schmechtig, C., Poteau, A., Leymarie, E., Dufour, A., Besson, F. and Obolensky, G.:
904 Seasonal variability of nutrient concentrations in the Mediterranean Sea: Contribution of Bio-Argo floats, *Journal of*
905 *Geophysical Research: Oceans*, 120, 8528–8550, doi:doi:10.1002/2015JC011103, 2015a.
- 906 Pasqueron de Fommervault, O., Migon, C., D’Ortenzio, F., Ribera d’Alcalá, M. and Coppola, L.: Temporal
907 variability of nutrient concentrations in the northwestern Mediterranean sea (DYFAMED time-series station), *Deep Sea*
908 *Research Part I: Oceanographic Research Papers*, 100, 1–12, doi:10.1016/j.dsr.2015.02.006, 2015b.
- 909 Pearson, K.: On lines and planes of closest fit to systems of points in space, *Philosophical Magazine Series 6*, 2(11),
910 559–572, doi:10.1080/14786440109462720, 1901.
- 911 Pollehne, F., Klein, B. and Zeitzschel, B.: Low light adaptation and export production in the deep chlorophyll
912 maximum layer in the northern Indian Ocean, *Deep Sea Research Part II: Topical Studies in Oceanography*, 40(3), 737–752,
913 doi:10.1016/0967-0645(93)90055-R, 1993.
- 914 Psarra, S., Tselepides, a. and Ignatiades, L.: Primary productivity in the oligotrophic Cretan Sea (NE Mediterranean):
915 seasonal and interannual variability, *Progress in Oceanography*, 46(2–4), 187–204, doi:10.1016/S0079-6611(00)00018-5,
916 2000.
- 917 Quéguiner, B., Tréguer, P., Peeken, I. and Scharek, R.: Biogeochemical dynamics and the silicon cycle in the Atlantic
918 sector of the Southern Ocean during austral spring 1992, *Deep-Sea Research Part II: Topical Studies in Oceanography*, 44(1–
919 2), 69–89, doi:10.1016/S0967-0645(96)00066-5, 1997.
- 920 Raimbault, P., Coste, B., Boulhadid, M. and Boudjellal, B.: Origin of high phytoplankton concentration in deep
921 chlorophyll maximum (DCM) in a frontal region of the Southwestern Mediterranean Sea (algerian current), *Deep-Sea*
922 *Research Part I*, 40(4), 791–804, doi:10.1016/0967-0637(93)90072-B, 1993.
- 923 Roesler, C., Uitz, J., Claustre, H., Boss, E., Xing, X., Organelli, E., Briggs, N., Bricaud, A., Schmechtig, C., Poteau,



- 924 A., D'Ortenzio, F., Ras, J., Drapeau, S., Haëntjens, N. and Barbieux, M.: Recommendations for obtaining unbiased
925 chlorophyll estimates from in situ chlorophyll fluorometers: A global analysis of WET Labs ECO sensors, *Limnology and*
926 *Oceanography: Methods*, 15(6), 572–585, doi:10.1002/lom3.10185, 2017.
- 927 Ryabov, A. B.: Phytoplankton competition in deep biomass maximum, *Theoretical Ecology*, 5(3), 373–385,
928 doi:10.1007/s12080-012-0158-0, 2012.
- 929 Sakamoto, C. M., Johnson, K. S. and Coletti, L. J.: Improved algorithm for the computation of nitrate concentrations
930 in seawater using an in situ ultraviolet spectrophotometer, *Limnology and Oceanography-Methods*, 7, 132–143,
931 doi:10.4319/lom.2009.7.132, 2009.
- 932 Sakamoto, C. M., Johnson, K. S., Coletti, L. J. and Jannasch, H. W.: Pressure correction for the computation of
933 nitrate concentrations in seawater using an in situ ultraviolet spectrophotometer, *Limnology and Oceanography: Methods*,
934 15(10), 897–902, doi:10.1002/lom3.10209, 2017.
- 935 Schmechtig, C., Poteau, A., Claustre, H., D'Ortenzio, F. and Boss, E.: Processing Bio-Argo chlorophyll-a
936 concentration at the DAC Level, *Argo Data Management*, 1–22, doi:10.13155/39468, 2015.
- 937 Schmechtig, C., Thierry, V. and The Bio-Argo Team: Argo Quality Control Manual for Biogeochemical Data, *Argo*
938 *Data Management*, 1–54, doi:10.13155/40879, 2016a.
- 939 Schmechtig, C., Poteau, A., Claustre, H., D'Ortenzio, F., Dall'Olmo, G. and Boss, E.: Processing Bio-Argo particle
940 backscattering at the DAC level Version, *Argo Data Management*, 1–13, doi:doi:10.13155/39459., 2016b.
- 941 Severin, T., Kessouri, F., Rembauville, M., Sánchez-Pérez, E. D., Oriol, L., Caparros, J., Pujo-Pay, M., Ghiglione,
942 Jean-François D'Ortenzio, F., Taillandier, V., Mayot, N., Durrieu De Madron, X., Ulses, C. and Estournel, Claude2, Conan,
943 P.: Open-ocean convection process: a driver of the winter nutrient supply and the spring phytoplankton distribution in the
944 Northwestern Mediterranean Sea, *Journal of Geophysical Research*, doi:10.1002/2014JC010094, 2017.
- 945 Siegel, D. A., Maritorena, S., Nelson, N. B. and Behrenfeld, M. J.: Independence and interdependencies among
946 global ocean color properties: Reassessing the bio-optical assumption, *Journal of Geophysical Research C: Oceans*, 110(7),
947 1–14, doi:10.1029/2004JC002527, 2005.
- 948 Siokou-Frangou, I., Christaki, U., Mazzocchi, M. G., Montresor, M., Ribera d'Alcalá, M., Vaqué, D. and Zingone,
949 a.: Plankton in the open Mediterranean Sea: a review, *Biogeosciences*, 7(5), 1543–1586, doi:10.5194/bg-7-1543-2010, 2010.
- 950 Stramski, D. and Kiefer, D. A.: Light scattering by microorganisms in the open ocean, *Progress in Oceanography*, 28,
951 343–383, 1991.
- 952 Stramski, D., Reynolds, R. A., Kahru, M. and Mitchell, B. G.: Estimation of Particulate Organic Carbon in the Ocean
953 from Satellite Remote Sensing, *Science*, 285(5425), 239–242, 1999.



- 954 Stramski, D., Bricaud, A. and Morel, A.: Modeling the inherent optical properties of the ocean based on the detailed
955 composition of the planktonic community, *Applied Optics*, 40(18), 2929–2945, doi:10.1364/AO.40.002929, 2001.
- 956 Stramski, D., Boss, E., Bogucki, D. and Voss, K. J.: The role of seawater constituents in light backscattering in the
957 ocean, *Progress in Oceanography*, 61(1), 27–56, doi:10.1016/j.pocean.2004.07.001, 2004.
- 958 Taillandier, V., Wagener, T., Ortenzio, F. D., Mayot, N., Legoff, H., Ras, J., Coppola, L., Pasqueron De
959 Fommervault, O., Diamond, E., Bittig, H., Lefevre, D., Leymarie, E., Poteau, A. and Prieur, L.: Hydrography in the
960 Mediterranean Sea during a cruise with RV Tethys 2 in May 2015, *Earth System Science Data*, (November), 1–30,
961 doi:10.17882/51678, 2017.
- 962 Tanhua, T., Hainbucher, D., Schroeder, K., Cardin, V., Álvarez, M. and Civitarese, G.: The Mediterranean Sea
963 system: a review and an introduction to the special issue, *Ocean Science*, 9(5), 789–803, doi:10.5194/os-9-789-2013, 2013.
- 964 Tripathy, S. C., Pavithran, S., Sabu, P., Pillai, H. U. K., Dessai, D. R. G. and Anilkumar, N.: Deep chlorophyll
965 maximum and primary productivity in Indian ocean sector of the southern ocean: Case study in the subtropical and polar
966 front during austral summer 2011, *Deep Sea Research Part II: Topical Studies in Oceanography*, 118, 240–249,
967 doi:10.1016/j.dsr2.2015.01.004, 2015.
- 968 Uitz, J., Claustre, H., Morel, A. and Hooker, S. B.: Vertical distribution of phytoplankton communities in open ocean:
969 An assessment based on surface chlorophyll, *Journal of Geophysical Research*, 111(C8), doi:10.1029/2005JC003207, 2006.
- 970 Uitz, J., Claustre, H., Griffiths, F. B., Ras, J., Garcia, N. and Sandroni, V.: A phytoplankton class-specific primary
971 production model applied to the Kerguelen Islands region (Southern Ocean), *Deep Sea Research Part I: Oceanographic
972 Research Papers*, 56(4), 541–560, doi:10.1016/j.dsr.2008.11.006, 2009.
- 973 Videau, C., Sourmia, A., Prieur, L. and Fiala, M.: Phytoplankton and primary production characteristics at selected
974 sites in the geostrophic Almeria-Oran front system (SW Mediterranean Sea), *Journal of Marine Systems*, 5(3–5), 235–250,
975 doi:10.1016/0924-7963(94)90049-3, 1994.
- 976 Westberry, T. K., Schultz, P., Behrenfeld, M. J., Dunne, J. P., Hiscock, M. R., Maritorea, S., Sarmiento, J. L. and
977 Siegel, D. A.: Annual cycles of phytoplankton biomass in the subarctic Atlantic and Pacific Ocean, *Global Biogeochemical
978 Cycles*, 30(2), 175–190, doi:10.1002/2015GB005276., 2016.
- 979 Whitmire, A. L., Pegau, W. S., Karp-Boss, L., Boss, E. and Cowles, T. J.: Spectral backscattering properties of
980 marine phytoplankton cultures, *Optics Express*, 18(14), 15073–15093, doi:10.1029/2003RG000148.D., 2010.
- 981 Winn, C. D., Campbell, L., Christian, J. R., Letelier, R. M., Hebel, D. V., Dore, J. E., Fujieki, L. and Karl, D. M.:
982 Seasonal variability in the phytoplankton community of the North Pacific Subtropical Gyre, *Global Biogeochemical Cycles*,
983 9(4), 605–620, doi:10.1029/95gb02149, 1995.
- 984 Zielinski, O., Voß, D., Saworski, B., Fiedler, B. and Körtzinger, A.: Computation of nitrate concentrations in turbid



985 coastal waters using an in situ ultraviolet spectrophotometer, *Journal of Sea Research*, 65(4), 456–460,
986 doi:10.1016/j.seares.2011.04.002, 2011.

987

988 **Figure captions**

989 **Figure 1:** Geographic location of the multi-variable vertical profiles collected by the BGC-Argo
990 profiling floats in the Mediterranean Sea. The boundaries of the regions considered in this study are
991 indicated by the black rectangles. NW, SW and TYR correspond to the Western Basin regions
992 whereas ION and LEV represent the Eastern Basin regions. The red color indicates BGC-Argo floats
993 equipped with nitrate sensors.

994 **Figure 2:** Comparison of the nitrate concentrations retrieved from the BGC-Argo floats to the
995 reference *in situ* measurements. The statistics (R^2 and slope) of the regression model between float
996 derived and *in situ* data are also indicated.

997 **Figure 3:** Boxplot of the distribution of the chlorophyll *a* concentration (Chl*a*) in the surface (a) and
998 SCM layers (b), the particulate backscattering coefficient (b_{bp}) in the SCM layer (c), and the depth (d)
999 and thickness (e) of the SCM for each Mediterranean region considered in this study.

1000 **Figure 4:** Monthly median value of the chlorophyll *a* concentration, Chl*a* (in green) and of the
1001 particulate backscattering coefficient, b_{bp} (in blue) in the SCM layer for the five Mediterranean regions
1002 considered in this study. The annual median of Chl*a* (0.28 mg m^{-3}) and b_{bp} ($5.8 \times 10^{-4} \text{ m}^{-1}$) calculated for
1003 the SCM layer and over the entire Mediterranean Sea are indicated by the green and blue horizontal
1004 lines, respectively. Note the different scales of the y-axes in panels a-e.

1005 **Figure 5:** Monthly median values of the Subsurface Chl*a* Maximum (in green), the nitracline (in
1006 black), the Subsurface b_{bp} Maximum (in blue) and our reference isolume (in yellow) for the five
1007 Mediterranean regions. The depth of the nitracline is not shown for the SW as there is no BGC-Argo
1008 float equipped with a nitrate sensor for this region.

1009 **Figure 6:** Boxplot of the distribution, for each of the Mediterranean regions considered in this study,
1010 of the difference between the depths of the nitracline $1 \mu\text{M}$ and of the isolume $0.3 \text{ mol quanta m}^{-2} \text{ d}^{-1}$



1011 (a), of the daily PAR in the SCM layer (b), and of the depth (c) and slope (d) of the nitracline. The SW
1012 is not always represented as there is no BGC-Argo float equipped with a nitrate sensor in this region.

1013 **Figure 7:** Normalized vertical profiles of the chlorophyll *a* concentration (Chl_a) (a, c, e, g, and i) and
1014 particulate backscattering coefficient (b_{bp}) (b, d, f, h, and j) for each of the considered Mediterranean
1015 regions. The Chl_a and b_{bp} are normalized to their individual profile maximum value, Chl_{a,max} and
1016 $b_{bp,max}$, respectively, while the depth is normalized to the euphotic depth (Z_{eu}). The color code indicates
1017 the different types of profiles, namely the different shapes are the “*bloom*”, “*mixed*”, “*SBM*”
1018 (Subsurface Biomass Maximum) with a distinction between the “*SBM_{aZeu}*” and the “*SBM_{bZeu}*” (for
1019 SBM occurring above or below the euphotic depth, respectively), and the “*SCM*” (Subsurface
1020 Chlorophyll Maximum) with a distinction between the “*SCM_{aZeu}*” and the “*SCM_{bZeu}*” (for SCM
1021 occurring or below the euphotic depth, respectively).

1022 **Figure 8:** Monthly occurrence of the different types of profiles shapes for each of the five considered
1023 Mediterranean regions. The color code indicates the type of profiles shape, namely “*bloom*”, “*mixed*”,
1024 “*SBM*” (Subsurface Biomass Maximum) with a distinction between the “*SBM_{aZeu}*” and the “*SBM_{bZeu}*”
1025 (for SBM occurring above or below the euphotic depth, respectively), and the “*SCM*” (Subsurface
1026 Chlorophyll Maximum) with a distinction between the “*SCM_{aZeu}*” and the “*SCM_{bZeu}*” (for SCM
1027 occurring or below the euphotic depth, respectively).

1028 **Figure 9:** Normalized vertical profiles of the chlorophyll *a* concentration (Chl_a) (a,c,e, and g) and
1029 particulate backscattering coefficient (b_{bp}) (b,d,f, and h) for each shape type. The Chl_a and b_{bp} are
1030 normalized to their individual profile maximum value, Chl_{a,max} and $b_{bp,max}$, respectively, while the
1031 depth is normalized to the euphotic depth (Z_{eu}). The color code and the type of lines indicate the
1032 region of the Mediterranean Sea and the different shapes, respectively. The different shapes are the
1033 “*bloom*”, “*mixed*”, “*SBM*” (Subsurface Biomass Maximum) with a distinction between the “*SBM_{aZeu}*”
1034 and the “*SBM_{bZeu}*” (for SBM occurring above or below the euphotic depth, respectively), and the
1035 “*SCM*” (Subsurface Chlorophyll Maximum) with a distinction between the “*SCM_{aZeu}*” and the
1036 “*SCM_{bZeu}*” (for SCM occurring or below the euphotic depth, respectively). Note the different scales of
1037 the x-axes.



1038 **Figure 10:** Trajectory and Chl*a* time series of the fGL (a-b) and fLS (c-d). On panels b and d, the
1039 white line shows the isolume $0.3 \text{ mol quanta m}^{-2} \text{ d}^{-1}$, the blue line indicates the Mixed Layer Depth
1040 (MLD) and the black line the nitracline $1 \mu\text{M}$.

1041 **Figure 11:** Nutrient versus light resource-limitation diagram for the two BGC-Argo floats deployed in
1042 the Gulf of Lions (a) and Levantine Sea (b). The color of the data points indicates the Chl*a*-to- b_{hp} ratio
1043 values. The x- and y-axes respectively represent the PAR and $[\text{NO}_3^-]$ values normalized to the
1044 maximum value calculated over the float lifetime in the layer extending from the surface to below the
1045 SCM. Note that the plots show only data collected within the SCM layer, thus corresponding to low
1046 normalized PAR values (i.e. under 25% of the maximum PAR).

1047 **Figure 12:** Schematic representation of the different situations of SCMs in the Mediterranean Sea for
1048 the five considered regions of the Mediterranean Sea along the west-to-east gradient.

1049

1050

1051

1052

1053

1054

1055

1056

1057

1058

1059

1060



1061

1062 **Table 1:** Regions with the corresponding abbreviation and number of available floats

1063 and profiles represented in the Mediterranean BGC-Argo database used in the present study

1064

Region	Basin	Abbreviation	Number of profiles	Number of floats
Gulf of Lions and Ligurian Sea	Western	NW	980	11
Algero-provencal Basin	Western	SW	540	5
Tyrrhenian Sea	Western	TYR	553	5
Ionian Sea	Eastern	ION	936	8
Levantine Sea	Eastern	LEV	1041	7
Total	2	5	4050	36

1065

1066

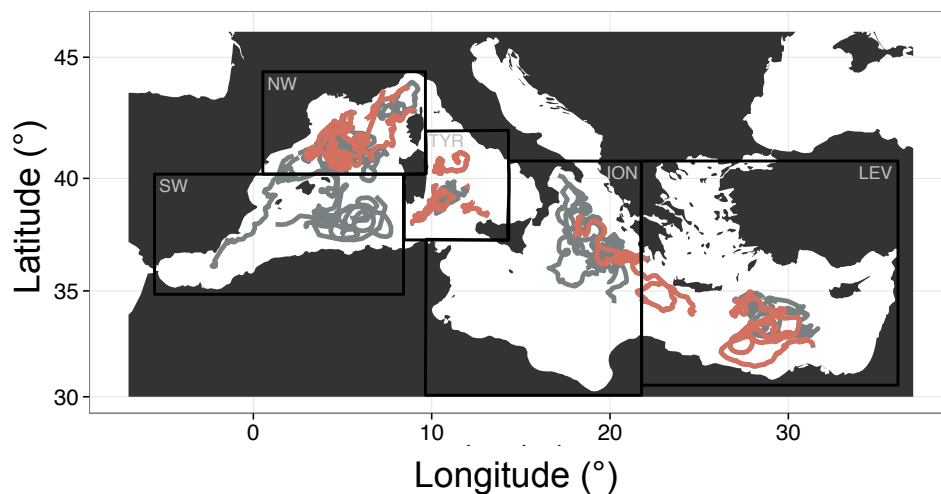
1067

1068

1069

1070

1071



1072

1073 **Figure 1:** Geographic location of the multi-variable vertical profiles collected by the BGC-Argo
1074 profiling floats in the Mediterranean Sea. The boundaries of the regions considered in this study are
1075 indicated by the black rectangles. NW, SW and TYR correspond to the Western Basin regions
1076 whereas ION and LEV represent the Eastern Basin regions. The red color indicates BGC-Argo floats
1077 equipped with nitrate sensors.

1078

1079

1080

1081

1082

1083

1084

1085



1086

1087

1088

1089

1090

1091

1092

1093

1094

1095

1096

1097

1098

1099 **Figure 2:** Comparison of the nitrate concentrations retrieved from the BGC-Argo floats to the

1100 reference *in situ* measurements. The statistics (R^2 and slope) of the regression model between float

1101 derived and *in situ* data are also indicated.

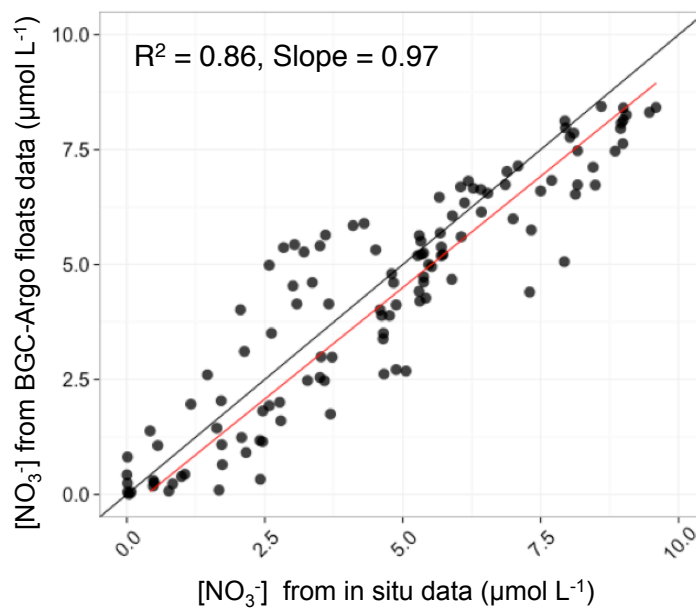
1102

1103

1104

1105

1106

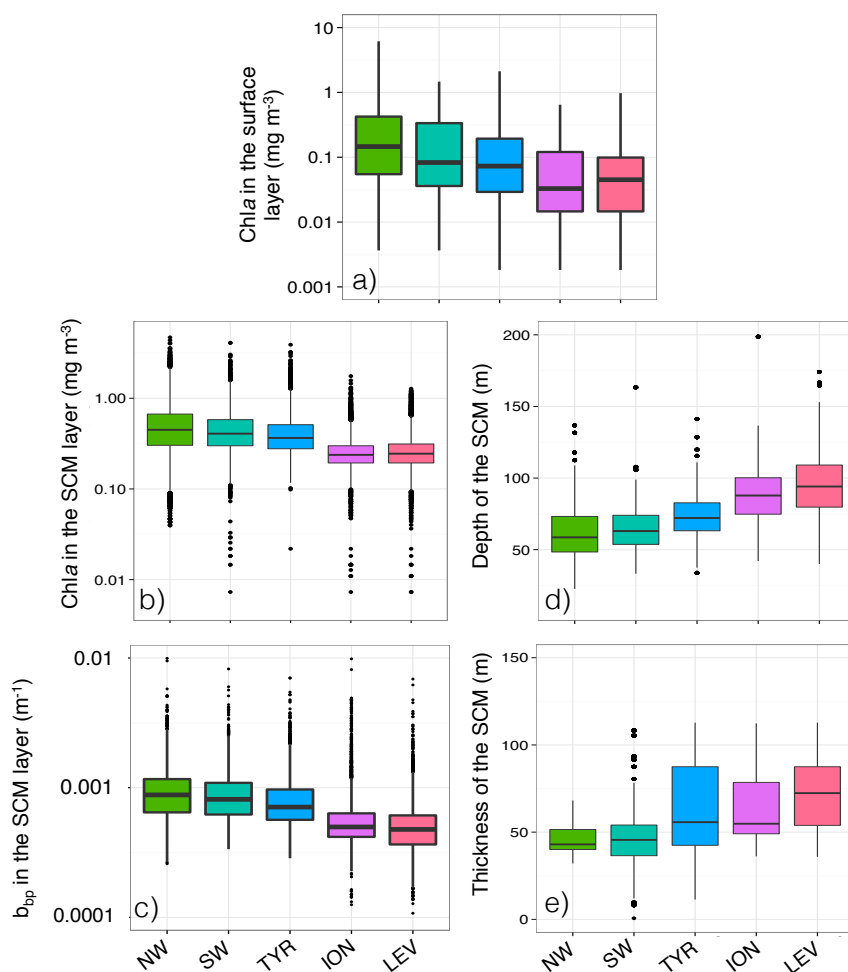




1107

1108

1109



1110

1111 **Figure 3:** Boxplot of the distribution of the chlorophyll *a* concentration (Chla) in the surface (a) and

1112 SCM layers (b), the particulate backscattering coefficient (b_{bp}) in the SCM layer (c), and the depth (d)

1113 and thickness (e) of the SCM for each Mediterranean region considered in this study.

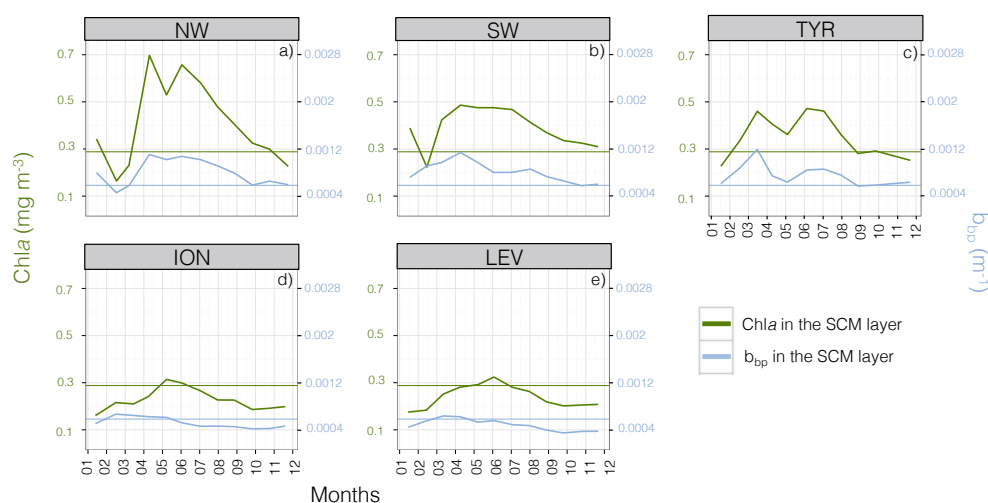
1114



1115

1116

1117



1118

1119 **Figure 4:** Monthly median value of the chlorophyll *a* concentration, Chla (in green) and of the
 1120 particulate backscattering coefficient, b_{bp} (in blue) in the SCM layer for the five Mediterranean regions
 1121 considered in this study. The annual median of Chla (0.28 mg m⁻³) and b_{bp} (5.8x10⁻⁴ m⁻¹) calculated for
 1122 the SCM layer and over the entire Mediterranean Sea are indicated by the green and blue horizontal
 1123 lines, respectively. Note the different scales of the y-axes in panels a-e.

1124

1125

1126

1127

1128

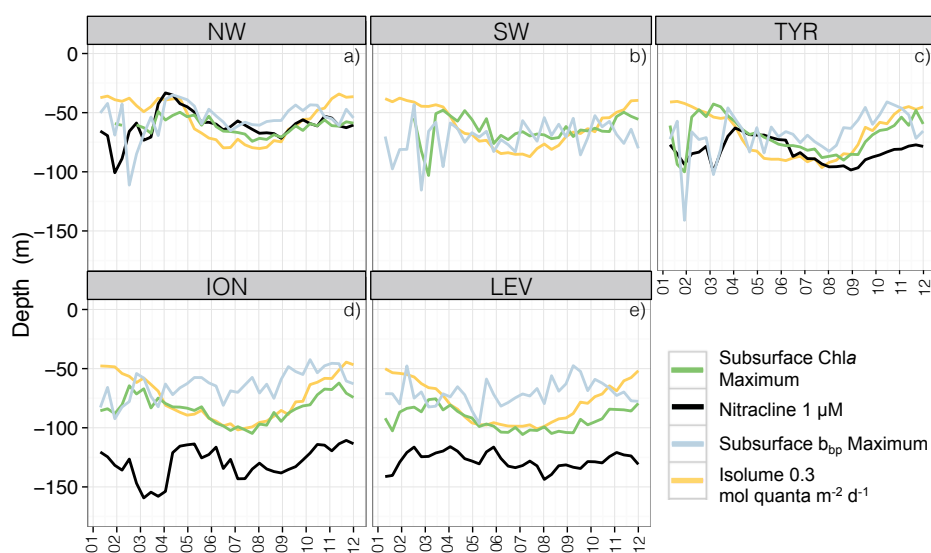
1129



1130

1131

1132



1133

1134 **Figure 5:** Monthly median values of the Subsurface Chla Maximum (in green), the nitracline (in

1135 black), the Subsurface b_{bp} Maximum (in blue) and our reference isolume (in yellow) for the five

1136 Mediterranean regions. The depth of the nitracline is not shown for the SW as there is no BGC-Argo

1137 float equipped with a nitrate sensor for this region.

1138

1139

1140

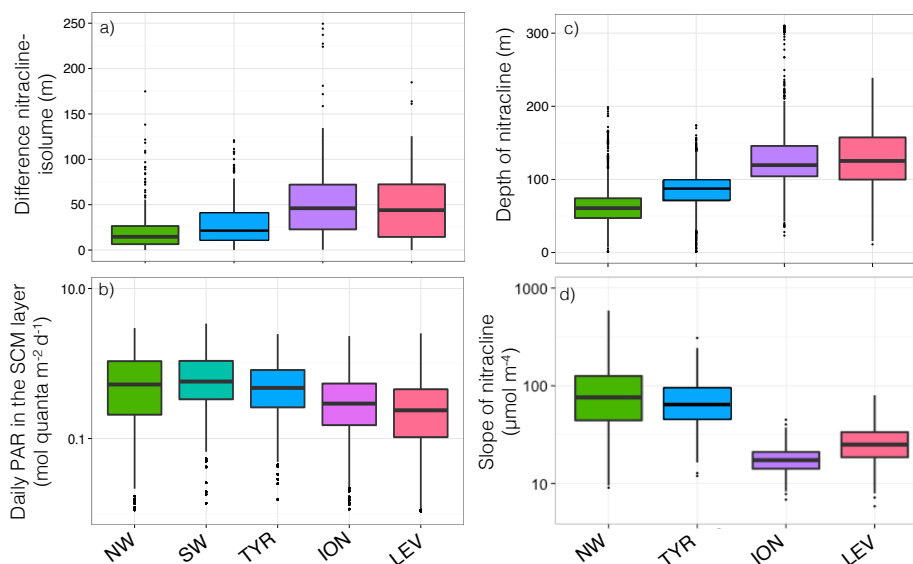
1141

1142

1143



1144



1145

1146

Figure 6: Boxplot of the distribution, for each of the Mediterranean regions considered in this study,

1147

of the difference between the depths of the nitracline 1 μM and of the isolume 0.3 mol quanta m⁻² d⁻¹

1148

(a), of the daily PAR in the SCM layer (b), and of the depth (c) and slope (d) of the nitracline. The SW

1149

is not always represented as there is no BGC-Argo float equipped with a nitrate sensor in this region.

1150

1151

1152

1153

1154

1155

1156

1157

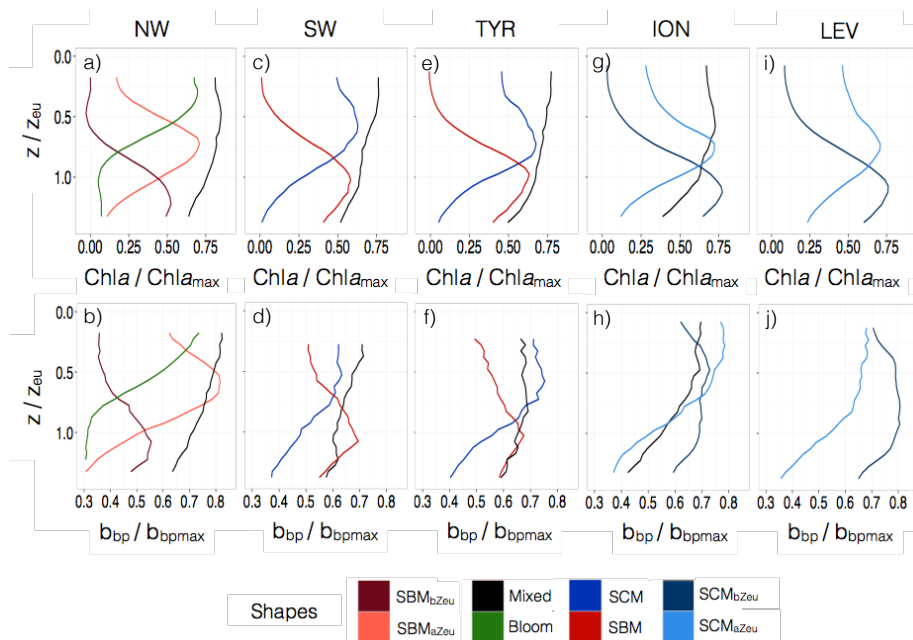


1158

1159

1160

1161

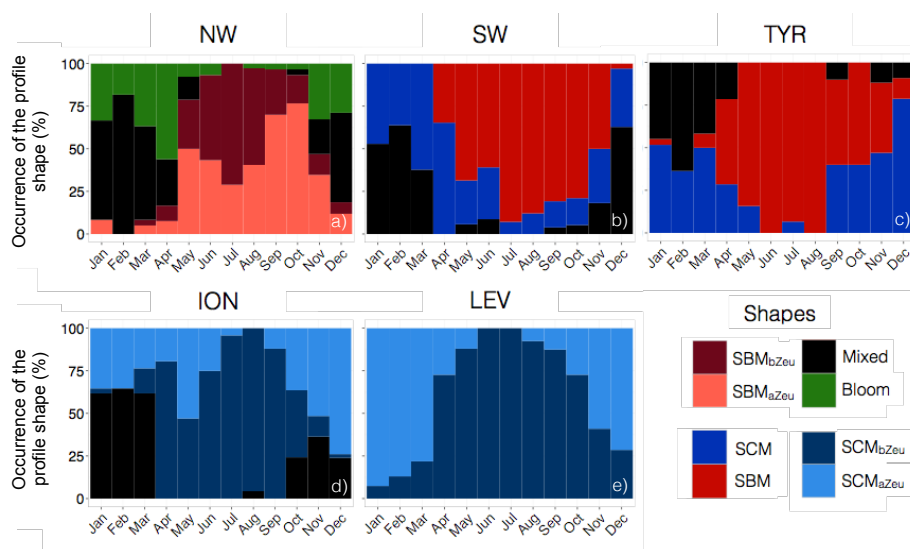


1162

1163 **Figure 7:** Normalized vertical profiles of the chlorophyll *a* concentration (Chla) (a, c, e, g, and i) and
 1164 particulate backscattering coefficient (b_{bp}) (b, d, f, h, and j) for each of the considered Mediterranean
 1165 regions. The Chla and b_{bp} are normalized to their individual profile maximum value, $Chla_{max}$ and
 1166 b_{bpmax} , respectively, while the depth is normalized to the euphotic depth (Z_{eu}). The color code indicates
 1167 the different types of profiles, namely the different shapes are the “bloom”, “mixed”, “SBM”
 1168 (Subsurface Biomass Maximum) with a distinction between the “ SBM_{aZeU} ” and the “ SBM_{bZeU} ” (for
 1169 SBM occurring above or below the euphotic depth, respectively), and the “SCM” (Subsurface
 1170 Chlorophyll Maximum) with a distinction between the “ SCM_{aZeU} ” and the “ SCM_{bZeU} ” (for SCM
 1171 occurring or below the euphotic depth, respectively).



1172



1173

1174 **Figure 8:** Monthly occurrence of the different types of profiles shapes for each of the five considered
 1175 Mediterranean regions. The color code indicates the type of profiles shape, namely “*bloom*”, “*mixed*”,
 1176 “*SBM*” (Subsurface Biomass Maximum) with a distinction between the “*SBM_{aZeu}*” and the “*SBM_{bZeu}*”
 1177 (for *SBM* occurring above or below the euphotic depth, respectively), and the “*SCM*” (Subsurface
 1178 Chlorophyll Maximum) with a distinction between the “*SCM_{aZeu}*” and the “*SCM_{bZeu}*” (for *SCM*
 1179 occurring or below the euphotic depth, respectively).

1180

1181

1182

1183

1184

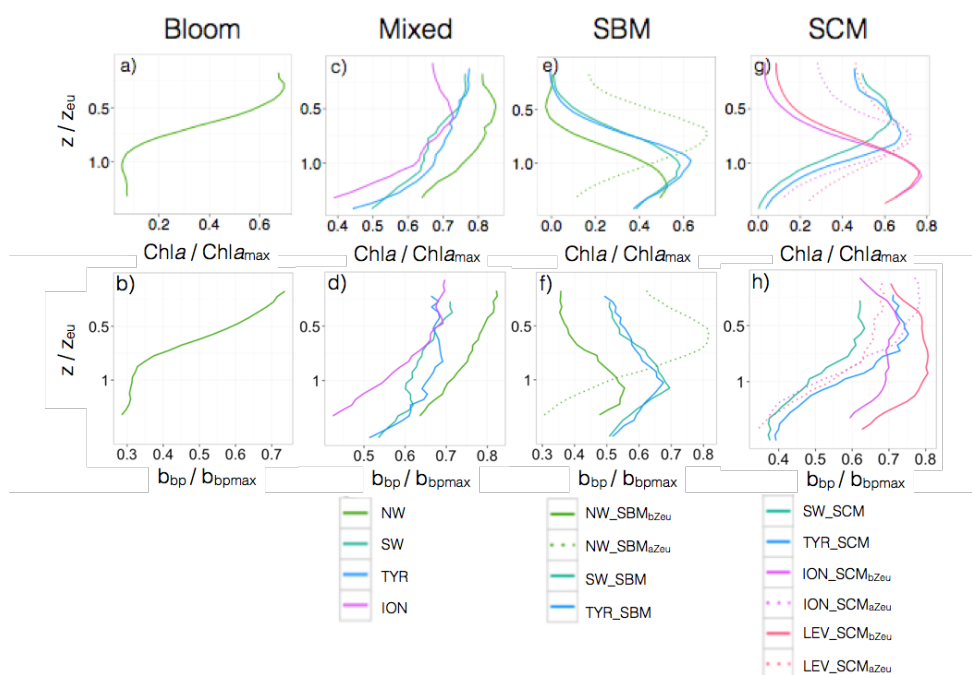
1185



1186

1187

1188



1189

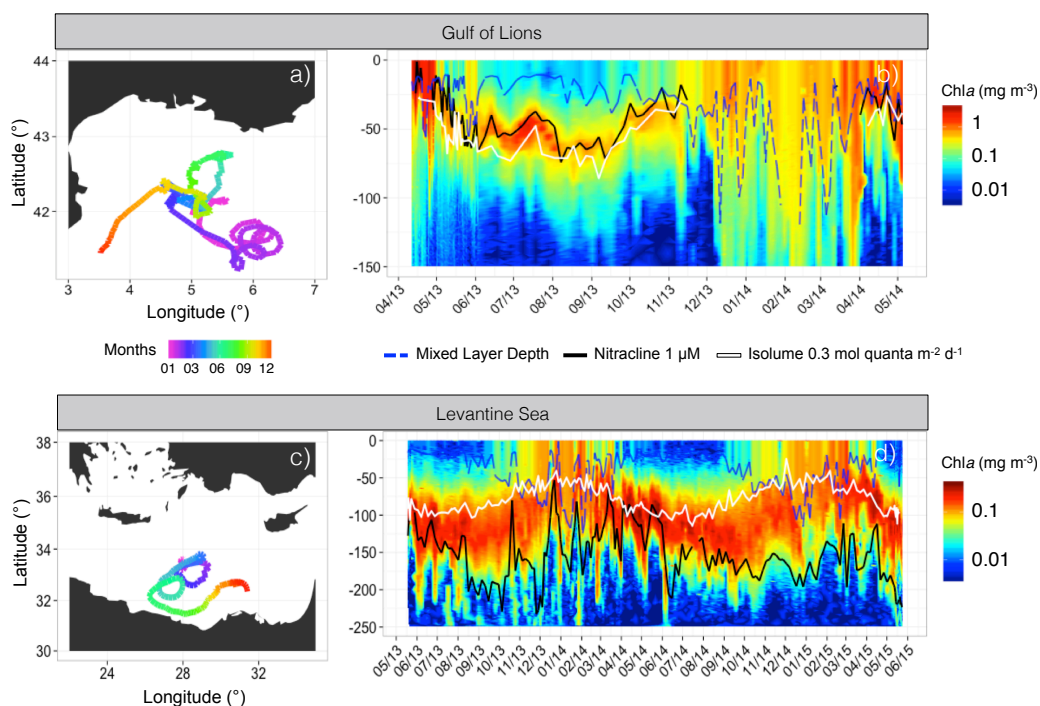
1190 **Figure 9:** Normalized vertical profiles of the chlorophyll *a* concentration (*Chla*) (a,c,e, and g) and
 1191 particulate backscattering coefficient (b_{bp}) (b,d,f, and h) for each shape type. The *Chla* and b_{bp} are
 1192 normalized to their individual profile maximum value, $Chla_{max}$ and b_{bpmax} , respectively, while the
 1193 depth is normalized to the euphotic depth (Z_{eu}). The color code and the type of lines indicate the
 1194 region of the Mediterranean Sea and the different shapes, respectively. The different shapes are the
 1195 “*bloom*”, “*mixed*”, “*SBM*” (Subsurface Biomass Maximum) with a distinction between the “*SBM_{aZeu}*”
 1196 and the “*SBM_{bZeu}*” (for SBM occurring above or below the euphotic depth, respectively), and the
 1197 “*SCM*” (Subsurface Chlorophyll Maximum) with a distinction between the “*SCM_{aZeu}*” and the
 1198 “*SCM_{bZeu}*” (for SCM occurring or below the euphotic depth, respectively). Note the different scales of
 1199 the x-axes.



1200

1201

1202



1203

1204 **Figure 10:** Trajectory and Chla time series of the fGL (a-b) and fLS (c-d). On panels b and d, the
1205 white line shows the isolume $0.3 \text{ mol quanta m}^{-2} \text{ d}^{-1}$, the blue line indicates the Mixed Layer Depth
1206 (MLD) and the black line the nitracline $1 \mu\text{M}$.

1207

1208

1209

1210

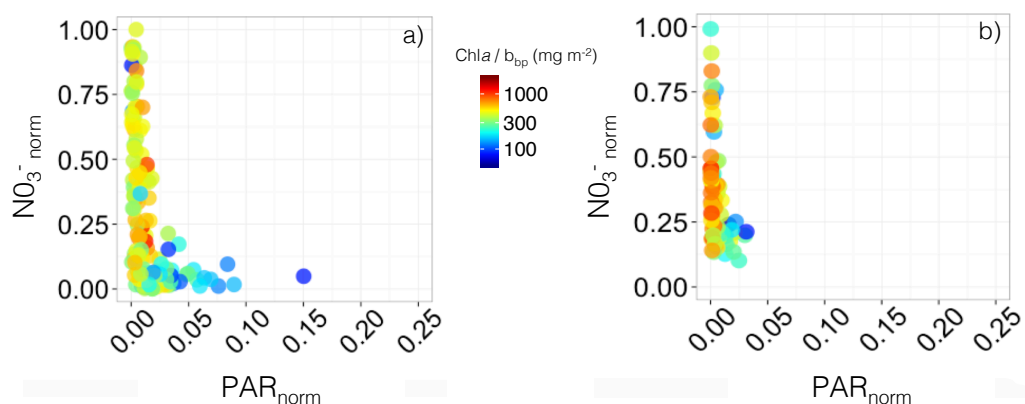
1211



1212

1213

1214



1215

1216 **Figure 11:** Nutrient versus light resource-limitation diagram for the two BGC-Argo floats deployed
 1217 in the Gulf of Lions (a) and Levantine Sea (b). The color of the data points indicates the $Chla$ -to- b_{bp}
 1218 ratio values. The x- and y-axes respectively represent the PAR and $[NO_3^-]$ values normalized to the
 1219 maximum value calculated over the float lifetime in the layer extending from the surface to below the
 1220 SCM. Note that the plots show only data collected within the SCM layer, thus corresponding to low
 1221 normalized PAR values (i.e. under 25% of the maximum PAR).

1222

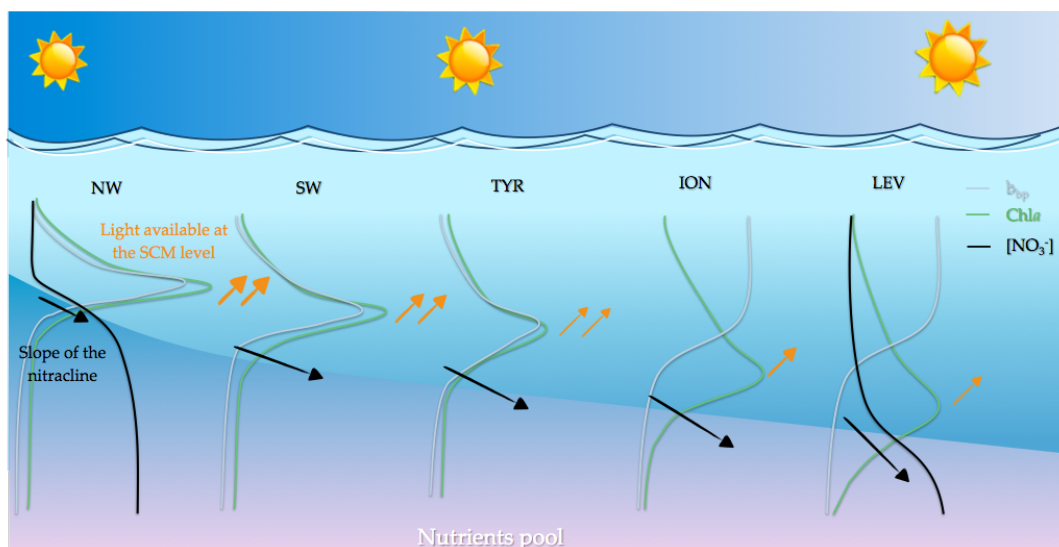
1223

1224

1225

1226

1227



1228

1229 **Figure 12:** Schematic representation of the different situations of SCMs in the Mediterranean Sea for
1230 the five considered regions of the Mediterranean Sea along the west-to-east gradient.

1231

1232

1233

1234